Resolving the PREX-CREX puzzle in covariant density functional theory

Mengying Qiu, ¹ Tong-Gang Yue, ² Zhen Zhang, ^{1,3,*} and Lie-Wen Chen^{2,†}

¹Sino-French Institute of Nuclear Engineering and Technology, Sun Yat-Sen University, Zhuhai 519082, China ²State Key Laboratory of Dark Matter Physics, Key Laboratory for Particle Astrophysics and Cosmology (MOE), and Shanghai Key Laboratory for Particle Physics and Cosmology, School of Physics and Astronomy, Shanghai Jiao Tong University, Shanghai, 200240, China ³Shanghai Research Center for Theoretical Nuclear Physics, NSFC and Fudan University, Shanghai, 200438, China (Dated: November 20, 2025)

The PREX-CREX puzzle, an apparent tension between parity-violating electron-scattering results for 208 Pb and 48 Ca revealed by modern density functional analyses, has posed a major challenge for nuclear theory. We show that this puzzle can be resolved within covariant density-dependent point-coupling density functional theory by introducing an enhanced isovector tensor coupling. A nonrelativistic reduction identifies the resulting strong isovector spin-orbit interaction as the key mechanism that reconciles the PREX and CREX measurements.

Introduction.—The neutron distribution in neutronrich nuclei is a fundamental nuclear structure property that encodes essential information on the equation of state (EOS) of asymmetric nuclear matter [1, 2]. Since the neutron carries significant (negative) weak charge, it also plays a critical role in nuclear weak-interaction processes, including coherent neutrino-nucleus scattering [3–6] and dark matter-nucleus scattering [7]. In particular, the neutron skin thickness $\Delta r_{\rm np}$, the difference between neutron and proton root-mean-square radii, has attracted considerable attention due to its strong correlation with the symmetry energy [8-22], making it crucial for both nuclear physics and astrophysics [23–34]. Experimentally, $\Delta r_{\rm np}$ is usually extracted through stronginteraction processes, which generally involve significant model dependence. Instead, parity-violating electron scattering (PVES) has been proposed as a unique and model-independent probe of $\Delta r_{\rm np}$ by measuring the parity-violating asymmetry and extracting the weak form factor $F_{\rm W}$. Recently, two high-precision PVES experiments at Jefferson Lab, PREX-II [35] on ²⁰⁸Pb and CREX [36] on ⁴⁸Ca, were performed to determine the charge-weak form-factor difference $\Delta F_{\rm CW}$ and thereby $\Delta r_{\rm np}$, but reported strikingly unexpected results. The PREX-II indicated a large $\Delta r_{\rm np}$ or $\Delta F_{\rm CW}$, which suggests an unusually stiff symmetry energy [35, 37], whereas CREX favored much softer nuclear symmetry energy. No existing theoretical models can reproduce both measurements within their 1σ uncertainties [36, 38–42]. This apparent inconsistency, known as the PREX-CREX puzzle, poses a major challenge for nuclear theory and calls into question our current understanding of weak and neutron distributions in nuclei.

Considerable efforts have been devoted to resolving the puzzle, but with limited success [43–47]. Very recently, within extended nonrelativistic Skyrme energy density functionals (EDFs), a strong isovector spin-orbit (IVSO) interaction has been proposed as a promising solution, motivated by the distinct shell structures of ⁴⁸Ca and

²⁰⁸Pb [48] (see also Ref. [49]). By enhancing the IVSO strength well beyond conventional Skyrme parametrizations, both PREX-II and CREX data can be simultaneously reproduced within their 1σ uncertainties without sacrificing basic nuclear properties [48]. This idea was further explored in Ref. [50], where the Dirac equation in relativistic mean-field (RMF) models was recast into an equivalent Schrödinger-like form to explicitly isolate the isovector component of the spin-orbit potential. Artificially increasing this component confirmed its strong influence on $\Delta r_{\rm np}$, but an excessively large IVSO potential led to level crossings of SO partners and even destroyed the magicity of ²⁰⁸Pb [50]. Therefore, although the strong IVSO interaction appears to be a promising mechanism, its quantitative role seems to depend on the model, and a consistent implication within covariant EDFs is still lacking.

In this letter, we show that the PREX-CREX puzzle can be resolved within covariant energy-density functionals by exploiting the connection between tensor couplings and the spin-orbit interaction [51–53]. Using a densitydependent point-coupling (DDPC) covariant EDF with tensor couplings, we construct three new parametrizations that simultaneously reproduce the PREX-II and CREX charge-weak form-factor differences in ²⁰⁸Pb and ⁴⁸Ca within their 1σ uncertainties, while maintaining reasonable description of nuclear ground-state properties and the empirical knowledge on nuclear EOS. A nonrelativistic reduction shows that the enhanced isovector tensor coupling in these new EDFs naturally generates a strong IVSO coupling, thereby reconciling the two experiments. Our results confirm the decisive role of the strong IVSO interaction and establish a consistent and physically grounded mechanism for its inclusion in covariant EDFs.

DDPC covariant density functional.— The conventional DDPC covariant EDF describes the nucleon-nucleon interaction through isoscalar-scalar (S), isoscalar-vector (V), and isovector-vector (τV)

four-fermion contact terms, along with a derivative term that accounts for leading finite-range effects [54]. In the present work, we employ an extended variant of the DDPC EDF that further includes isovector-scalar (τS) , isoscalar-tensor (T), and isovector-tensor (τT) couplings, following Ref. [55]. The effective Lagrangian density reads [55]

$$\mathcal{L} = \bar{\psi} \left(i \gamma_{\mu} \partial^{\mu} - m \right) \psi - e \frac{1 - \tau_{3}}{2} \bar{\psi} \gamma_{\mu} \psi A^{\mu} - \frac{1}{4} F_{\mu\nu} F^{\mu\nu}
- \frac{1}{2} \alpha_{S} (\bar{\psi} \psi)^{2} - \frac{1}{2} \alpha_{\tau S} (\bar{\psi} \vec{\tau} \psi)^{2} - \frac{1}{2} \alpha_{V} (\bar{\psi} \gamma_{\mu} \psi)^{2}
- \frac{1}{2} \alpha_{\tau V} (\bar{\psi} \gamma_{\mu} \vec{\tau} \psi)^{2} - \frac{1}{2} \alpha_{T} (\bar{\psi} \sigma_{\mu\nu} \psi)^{2} - \frac{1}{2} \alpha_{\tau T} (\bar{\psi} \sigma_{\mu\nu} \vec{\tau} \psi)^{2}
- \frac{1}{2} \delta_{S} \partial_{\mu} (\bar{\psi} \psi) \partial^{\mu} (\bar{\psi} \psi). \tag{1}$$

Here ψ denotes the nucleon field, m is the nucleon mass, $\vec{\tau}$ the isospin Pauli matrices with $\tau_3 = 1(-1)$ for neutrons (protons), and A^{μ} and $F^{\mu\nu}$ are the four-vector potential and field tensor of the electromagnetic field, respectively. The scalar, vector, isovector-scalar, and isovector-vector couplings, $\alpha_{\rm S}$, $\alpha_{\tau \rm S}$, $\alpha_{\rm V}$, and $\alpha_{\tau \rm V}$, are taken as density-dependent and parameterized as

$$\alpha_i(\rho) = \alpha_i(\rho_{\text{sat}}) f_i(x), \text{ for i = S, } \tau \text{S, V, } \tau \text{V},$$
 (2)

where

$$f_i(x) = a_i \frac{1 + b_i(x + d_i)^2}{1 + c_i(x + d_i)^2}$$
 (3)

is a function of $x = \rho/\rho_{\rm sat}$ with ρ being the baryon density, and $\rho_{\rm sat} = 0.156~{\rm fm}^{-3}$ being the saturation density of symmetric nuclear matter. By construction, $f_i(1) = 1$ and the additional constraint $f_i''(0) = 0$ is imposed [55, 56]. The isoscalar-tensor, isovector-tensor, and derivative couplings, $\alpha_{\rm T}$, $\alpha_{\tau \rm T}$, and $\delta_{\rm S}$, are assumed to be density independent. In Ref. [55], the relation $\alpha_{\tau \rm T} = (\alpha_{\rm S} + 3\alpha_{\tau \rm S} + 2\alpha_{\rm V} - 6\alpha_{\tau \rm V} + 6\alpha_{\rm T})/18$ was imposed by the Fierz transformation, which recasts the exchange (Fock) contributions into Hartree-type local contact terms within the point-coupling framework. In the present work, however, we treat $\alpha_{\tau \rm T}$ as a free parameter to explore the impact of the isovector tensor coupling.

Starting from the well-calibrated DDPC EDF PCF-PK1 [55], we keep $\alpha_{\rm S}(\rho)$ and $\alpha_{\rm V}(\rho)$ unchanged, since the $\Delta F_{\rm CW}$ and $\Delta r_{\rm np}$ are largely insensitive to the isoscalar sector. The remaining nine parameters, $\alpha_{\tau \rm S}(\rho_{\rm sat})$, $a_{\tau \rm S}$, $d_{\tau \rm S}$, $\alpha_{\tau \rm V}(\rho_{\rm sat})$, $a_{\tau \rm V}$, $d_{\tau \rm V}$, $\alpha_{\tau \rm T}$, $\alpha_{\rm T}$, and $\delta_{\rm S}$, are optimized by fitting to both the PREX-II and CREX data as well as other empirical data (see following). As emphasized by the CREX collaboration [36], the extraction of $\Delta r_{\rm np}$ in 48 Ca is subject to sizable model dependence. We therefore focus on the experimentally determined difference between the charge and weak form factors, $\Delta F_{\rm CW}(q) \equiv F_{\rm C}(q) - F_{\rm W}(q)$, at the measured momentum transfers: $\Delta F_{\rm CW}^{208}(q=0.3977~{\rm fm}^{-1}) = 0.041 \pm 0.013~{\rm for}^{208}{\rm Pb}$ [35]

and $\Delta F_{\rm CW}^{48}(q=0.8733~{\rm fm}^{-1})=0.0277\pm0.0055$ for $^{48}{\rm Ca}$ [36]. The charge and weak form factors are calculated following Refs. [21, 57], including both vector-density and spin-orbit current contributions (see Supplemental Material (SM) Sec. S.I for details).

In addition to $\Delta F_{\rm CW}^{208}$ and $\Delta F_{\rm CW}^{48}$, the fit includes the binding energies $E_{\rm B}$ and charge radii $R_{\rm c}$ of $^{48}{\rm Ca}$ and ²⁰⁸Pb, the spin-orbit splittings $\Delta \epsilon_{ls}$ of the $\nu 1f$ orbital in 48 Ca and of the $\pi 2d$, $\nu 3p$, and $\nu 2f$ orbitals in ²⁰⁸Pb [39, 58, 59], the symmetry energy at two-thirds saturation density, $E_{\text{sym}}(2\rho_{\text{sat}}/3) = 25.6^{+1.4}_{-1.3} \text{ MeV from}$ nuclear masses [60], and the pure neutron matter equation of state around $\rho_{\rm sat}/3$, $E_{\rm PNM}(\rho = 0.04805~{\rm fm}^{-3}) =$ 6.72 ± 0.08 MeV from chiral effective field theory [61]. (1) By sampling the parameter space (see SM Sec. S.II for details), we construct three new EDFs, ZH-1, ZH-2, and ZH-3, each exhibiting distinct density dependence of the symmetry energy. The corresponding coupling constants are listed in Tab. I together with those of PCF-PK1 for comparison. Remarkably, in all ZH EDFs, the isovectortensor coupling $\alpha_{\tau T}$ is significantly enhanced relative to PCF-PK1.

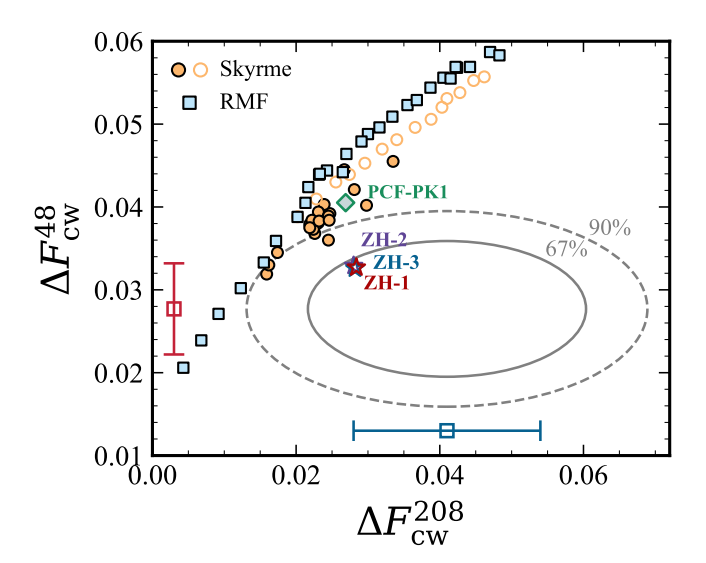


FIG. 1. Predicted charge-weak form-factor differences $\Delta F_{\rm CW}^{48}$ and $\Delta F_{\rm CW}^{208}$ for $^{48}{\rm Ca}$ and $^{208}{\rm Pb}$ from the three newly constructed covariant EDFs: ZH-1, ZH-2, and ZH-3 (open stars). For comparison, results from PCF-PK1 [55] (diamonds), other covariant EDFs [36] (squares), and nonrelativistic Skyrme-like EDFs [36, 62] (circles) are also shown. The solid (dashed) ellipse indicates the joint 67% (90%) confidence contour from the PREX-II and CREX measurements. Experimental values are shown with error bars, corresponding to $\Delta F_{\rm CW}^{208}(q=0.3977~{\rm fm}^{-1})=0.041\pm0.013~{\rm from~PREX-II}$ [35] and $\Delta F_{\rm CW}^{48}(q=0.8733~{\rm fm}^{-1})=0.0277\pm0.0055~{\rm from~CREX}$ [36].

Resolution of the PREX-CREX puzzle.— In Fig. 1, we display the predicted charge-weak form-factor differences $\Delta F_{\rm CW}^{48}$ and $\Delta F_{\rm CW}^{208}$ for ⁴⁸Ca and ²⁰⁸Pb, respec-

TABLE I. Values of model parameters and predictions of the three new EDFs, ZH-1, ZH-2, and ZH-3, in comparison with PCF-PK1 [55]. Predictions are shown for the charge-weak form-factor difference $\Delta F_{\rm CW}$ and the neutron skin thickness $\Delta r_{\rm np}$ in ⁴⁸Ca and ²⁰⁸Pb, as well as the symmetry energy $E_{\text{sym}}(\rho)$ and its density slope parameter $L(\rho)$ at ρ_{sat} and $2\rho_{\rm sat}/3$. The last six rows list the density-averaged isoscalar, isovector, and mixed spin-orbit strengths, $\langle b_{\rm IS} \rangle$, $\langle b_{\rm IV} \rangle$, and $\langle b_{\rm SV} \rangle$ in ⁴⁸Ca and ²⁰⁸Pb, derived from the nonrelativistic reduction. The parameters $\alpha_{\tau S}(\rho_{sat})$, $\alpha_{\tau V}(\rho_{sat})$, α_{T} , and $\alpha_{\tau T}$ are in fm², while $\delta_{\rm S}$ is in fm⁴. $\Delta r_{\rm np}$ values are in fm; $E_{\rm sym}$ and L are in MeV; $\langle b_{\rm IS} \rangle$, $\langle b_{\rm IV} \rangle$, and $\langle b_{\rm SV} \rangle$ are in MeV · fm⁵. The superscripts "48" and "208" indicate results for ⁴⁸Ca and ²⁰⁸Pb, respectively. All four EDFs share identical parameters in the isoscalar sector: $\alpha_{\rm S}(\rho_{\rm sat}) = -6.315 \text{ fm}^2$, $a_{\rm S} = 1.425$, $b_{\rm S} = 0.3185, c_{\rm S} = 0.5929, d_{\rm S} = 0.7498, \alpha_{\rm V}(\rho_{\rm sat}) = 3.533 \text{ fm}^2,$ $a_{\rm V} = 0.8076, b_{\rm V} = 0.06058, c_{\rm V} = 0.03693, d_{\rm V} = 3.005.$

-				
	PCF-PK1	ZH-1	ZH-2	ZH-3
$\alpha_{\tau S}(\rho_{\rm sat})$	-1.981	-4.701	-0.8403	-3.321
$a_{ au ext{S}}$	2.328	0.5947	2.126	1.802
$b_{ au ext{S}}$	0.06179	84.914	334.1	9.290
$c_{ au ext{S}}$	0.5704	50.16	711.5	17.36
$d_{ au ext{S}}$	0.7644	0.08152	0.02165	0.1386
$lpha_{ au ext{V}}(ho_{ ext{sat}})$	2.976	5.400	1.927	4.096
$a_{ au} { m v}$	2.547	4.212	9.430	6.656
$b_{ au ext{V}}$	0.3459	-0.001241	-0.001728	-0.002950
$c_{ au ext{V}}$	1.612	0.0006678	0.0007385	0.001406
$d_{ au ext{V}}$	0.4547	22.34	21.24	15.39
$\delta_{ m S}$	-0.6658	-0.7173	-0.7886	-0.7311
$lpha_{ m T}$	3.374	4.312	5.673	4.546
$lpha_{ au\mathrm{T}}$	0.535^{a}	6.967	9.195	7.114
$\Delta F_{\mathrm{CW}}^{48}$	0.0405	0.0327	0.0329	0.0326
$\Delta F_{ m CW}^{208}$	0.0269	0.0284	0.0280	0.0282
$\Delta r_{ m np}^{48}$	0.172	0.116	0.128	0.127
$\Delta r_{ m np}^{208}$	0.183	0.188	0.190	0.191
$E_{\mathrm{sym}}(\dot{\rho}_{\mathrm{sat}})$	33.0	33.6	32.4	32.1
$E_{\rm sym}(2\rho_{\rm sat}/3)$	24.5	25.4	25.8	26.9
$L(ho_{ m sat})$	78.4	66.7	43.8	19.4
$L(2\rho_{\mathrm{sat}}/3)$	50.4	54.2	50.2	49.0
$\langle b_{\mathrm{IS}}^{(48)} \rangle$	150	172	205	178
$\langle b_{\mathrm{IS}}^{(208)} \rangle$	153	176	210	182
$\langle b_{\mathrm{IV}}^{(48)} \rangle$	35.0	222	230	213
$\langle b_{\mathrm{IV}}^{(208)} \rangle$	36.7	229	238	219
$\langle b_{ m SV}^{(48)} angle$	1.48	-0.302	0.0502	0.668
$\langle b_{ m SV}^{(208)} angle$	2.22	-0.349	0.0503	0.807

 $^{^{\}rm a}$ The maximum value of $\alpha_{\tau{\rm T}}$ in $^{48}{\rm Ca}$ in PCF-PK1.

tively, obtained with various covariant and nonrelativistic EDFs [36, 62]. The results of the three ZH EDFs are shown as open stars and listed in Tab. I. As seen, while all other EDFs lie outside the 67% confidence ellipse of the CREX and PREX-II measurements, the three new EDFs reproduce both $\Delta F_{\rm CW}^{48}$ and $\Delta F_{\rm CW}^{208}$ within their respective 1σ uncertainties. Particularly, compared with the PCF-PK1, the three new EDFs predict very similar $\Delta F_{\rm CW}^{208}$ but much less $\Delta F_{\rm CW}^{48}$.

Previous attempts to reconcile the tension between the PREX-II and CREX results have achieved similar improvements by extending nonlinear relativistic mean-field models to allow a more flexible density dependence of the symmetry energy [45, 46, 63]. However, such modifications come at a significant cost, leading to unrealistically stiff symmetry energies that contradict both empirical knowledge and *ab initio* predictions, and/or unphysical density fluctuations in the nuclear interior.

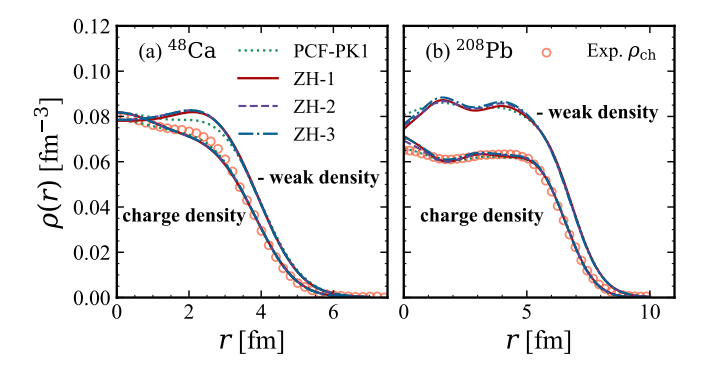


FIG. 2. The charge (solid lines) and weak (dashed lines) radial density distributions in 48 Ca (a) and 208 Pb (b) predicted by ZH-1 (red), ZH-2 (purple), ZH-3 (blue), and PCF-PK1 (green). Experimental charge densities [64] are shown as open circles.

We therefore show in Fig. 2 the radial distributions of charge and weak densities in ⁴⁸Ca and ²⁰⁸Pb predicted by the ZH family, compared with those from PCF-PK1 and the experimental charge-density data [64]. All three new EDFs reproduce the charge densities satisfactorily and show no spurious core fluctuations. For ⁴⁸Ca, the weak density deviates from PCF-PK1 mainly in the surface region, whereas for ²⁰⁸Pb it remains nearly unchanged, consistent with the $\Delta F_{\rm CW}$ behavior shown in Fig. 1. We further access the performance of the three new EDFs in describing the equation of state of pure neutron matter, $E_{\rm PNM}(\rho)$, and the ground states properties of representative (semi-)doubly magic nuclei. The predicted $E_{\rm PNM}(\rho)$ agrees well with results from chiral effective field theory, and the calculated binding energies and charge radii of most (semi-)doubly magic nuclei reproduce experimental data within relative deviations of less than 1%, except for the light nuclei ¹⁶O and ⁴⁰Ca (see SM Sec. S.III for details).

Inspired by the strong IVSO mechanism proposed in Ref. [48], we perform a nonrelativistic reduction of the covariant potential energy density to identify the connection between tensor couplings and spin-orbit interactions. By expanding the potential energy density in powers of $\mathcal{B}_0 = 1/(2m^*)$, where m^* denotes the isoscalar Dirac effective mass, and retaining terms up to \mathcal{B}_0^2 , the spin-orbit part of the reduced energy density can be expressed as

$$\mathcal{E}_{SO} = \frac{b_{IS}}{2} \nabla \rho \cdot \boldsymbol{J} + \frac{b_{IV}}{2} \nabla \tilde{\rho} \cdot \tilde{\boldsymbol{J}} + \frac{b_{SV}}{2} \nabla \rho \cdot \tilde{\boldsymbol{J}}, \quad (4)$$

where $b_{\rm IS}=8\mathcal{B}_0^2\alpha_{\rm T}-4\mathcal{B}_0^2\left[\alpha_{\rm S}(\rho)+\alpha_{\rm S}'(\rho)\rho\right],\ b_{\rm IV}=8\mathcal{B}_0^2\alpha_{\tau \rm T}-4\mathcal{B}_0^2\alpha_{\tau \rm S}(\rho),\ {\rm and}\ b_{\rm SV}=-4\mathcal{B}_0^2\alpha_{\tau \rm S}'(\rho)\tilde{\rho}.$ Here

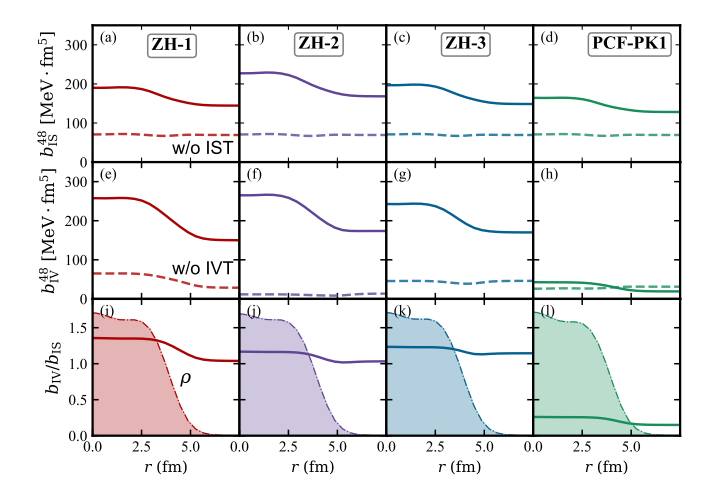


FIG. 3. Radial dependence of the isoscalar and isovector spin-orbit strength parameters, $b_{\rm IS}$ (top panels) and $b_{\rm IV}$ (middle panels), together with their ratio (bottom panels) in 48 Ca, obtained from the nonrelativistic reduction of the ZH-1 (red), ZH-2 (purple), ZH-3 (blue), and PCF-PK1 (green) covariant EDFs. Dashed lines labeled "w/o IST (w/o IVT)" denote the results obtained without the corresponding tensor terms. The shaded region in the bottom panels indicate the nucleon density distributions in 48 Ca.

 $\rho = \rho_n + \rho_p \ (\tilde{\rho} = \rho_n - \rho_p)$ and $\mathbf{J} = \mathbf{J}_n + \mathbf{J}_p \ (\tilde{\mathbf{J}} = \mathbf{J}_n - \mathbf{J}_p)$ are the isoscalar (isovector) densities and spin-orbit densities, respectively. Compared with the nonrelativistic Skyrme form, this expression shows explicit density dependences in the isoscalar and isovector SO coupling parameters $b_{\rm IS}$ and $b_{\rm IV}$, and includes an additional $b_{\rm SV}$ term arising from the density dependence of $\alpha_{\tau S}$.

The density-weighted averages $\langle b_{\rm IS} \rangle$, $\langle b_{\rm IV} \rangle$, and $\langle b_{\rm SV} \rangle$ for $^{48}{\rm Ca}$ and $^{208}{\rm Pb}$ obtained with the ZH family and PCF-PK1 are summarized in Tab. I. The quantity $b_{\rm SV}$ is numerically small, so the dominant contributions arise from the $b_{\rm IS}$ and $b_{\rm IV}$. Relative to PCF-PK1, $\langle b_{\rm IS} \rangle$ in the ZH family increases only moderately (by a few tens of percent), whereas $\langle b_{\rm IV} \rangle$ is enhanced by roughly a factor of six.

Figure 3 displays the radial profiles of $b_{\rm IS}$, $b_{\rm IV}$, and their ratio $b_{\rm IV}/b_{\rm IS}$ in $^{48}{\rm Ca}$ for ZH-1, ZH-2, ZH-3, and PCF-PK1 (solid lines). To isolate the contribution of tensor couplings, the dashed lines show $b_{\rm IS}$ calculated without the isoscalar tensor coupling ("w/o IST") and $b_{\rm IV}$ calculated without the isovector tensor coupling ("w/o IVT"). In the ZH family, the strong isovector tensor coupling produces a pronounced enhancement of $b_{\rm IV}$, while $b_{\rm IS}$ is only moderately affected by isoscalar tensor coupling. Consequently, the ratio $b_{\rm IV}/b_{\rm IS}$ increases from about 1/3 in PCF-PK1 to above unity. The results for $^{208}{\rm Pb}$ (not shown) follow the same qualitative trend, with only minor quantitative differences.

The resolution of the PREX-CREX puzzle in the ZH family can thus be traced to the strong IVSO interaction introduced through the enhanced isovector tensor cou-

pling. Due to their different shell structures, the effect of $b_{\rm IV}$ differs significantly between ⁴⁸Ca and ²⁰⁸Pb. In spherical nuclei, orbitals with total angular momentum $j_{>}=l+\frac{1}{2}$ contribute positively to the spin-orbit density **J**, while their partners with $j_{<} = l - \frac{1}{2}$ contribute negatively. In ²⁰⁸Pb, the dominant contributions from the unpaired neutron $1h_{11/2}$ and proton $1i_{13/2}$ orbitals largely cancel, leading to a small \tilde{J} and weak sensitivity to $b_{\rm IV}$. In contrast, in ⁴⁸Ca all proton spin-orbit partners are filled, and the eight unpaired neutrons in $1f_{7/2}$ generate a large positive J_n , yielding a sizable \tilde{J} and an amplified response to $b_{\rm IV}$. In agreement with the nonrelativistic Skyrme-like EDF results [48], the enhanced $b_{\rm IV}$ in the ZH family markedly reduces $\Delta F_{\rm CW}^{48}$, whereas $\Delta F_{\rm CW}^{208}$ remains essentially unchanged, thereby resolving the PREX-CREX puzzle.

Recently, the importance of the IVSO potential was also confirmed by equivalent Schrödinger-like analyses of meson-exchange RMF models [50]. That study also raised concerns that the large IVSO potential required to reproduce the PREX2 and CREX data could invert spin-orbit partner levels and even spoil the magicity of ²⁰⁸Pb. To address this concern, we examined the single-particle spectra of ⁴⁸Ca and ²⁰⁸Pb predicted by the ZH EDFs and found that the ordering of spin-orbit partner levels near the Fermi surface, as well as the magicity of ⁴⁸Ca and ²⁰⁸Pb, remain intact (see SM Sec. S.III).

It should be emphasized that, in a consistent treatment of the strong IVSO interaction employed in this work, the $b_{\rm IV}$ term contributes not only to the single-particle spin-orbit potential but also to the average central mean field. If the spin-orbit potential were the main driver of the change in $\Delta F_{\rm CW}^{48}$, one would expect dominant effects from high-l orbitals [50] and opposite contributions from spin-orbit partners. Our orbital-by-orbital decomposition of $\Delta F_{\rm CW}$ shows neither behavior. This indicates that the dominant effect of $b_{\rm IV}$ arises through modifications of the central mean-field rather than the spin-orbit potential (see SM Sec. S.IV and also Ref. [48]).

Neutron skin thickness and the symmetry energy.— Also listed in Tab. I are the predicted neutron skin thicknesses of ⁴⁸Ca and ²⁰⁸Pb, together with the symmetry energy $E_{\text{sym}}(\rho)$ and its density slope parameter $L(\rho)$ at $\rho_{\rm sat}$ and $2\rho_{\rm sat}/3$. Notably, ZH family predicts nearly identical $\Delta r_{\rm np}^{208}$ even though their $L(\rho_{\rm sat})$ values differ substantially from 19.4 to 66.7 MeV, breaking the wellknown $\Delta r_{\rm np}^{208}$ -L correlation. Similar trends have been reported in Refs. [45, 63], where covariant EDFs were modified to introduce more flexible density dependences of the symmetry energy. In contrast to the large variation in $L(\rho_{\rm sat})$, the $L(2\rho_{\rm sat}/3)$ remains almost unchanged among the three ZH EDFs. This indicates that the robust $\Delta r_{\rm np}^{208}$ - $L(2\rho_{\rm sat}/3)$ correlation proposed in Ref. [16] persists even after incorporating a strong isovector-tensor coupling (see SM Sec. S.V). Unlike $\Delta r_{\rm np}^{208}$, the neutron skin thickness of 48 Ca is strongly sensitive to both the IVSO interaction and the density dependence of the symmetry energy. Once the symmetry energy is well constrained, the $\Delta r_{\rm np}^{48}$ could serve as an effective probe of the strength of the IVSO interaction.

Summary.— We have shown that the PREX-CREX puzzle can be resolved within covariant energy density functional theory by introducing a strong isovector tensor coupling without sacrificing fundamental nuclear properties. A nonrelativistic reduction reveals that the enhanced isovector tensor coupling significantly increases the strength $b_{\rm IV}$ of the IVSO interaction, leading to a large reduction of $\Delta F_{\rm CW}^{48}$ without significantly affecting $\Delta F_{\rm CW}^{208}$. The sensitivity of $\Delta F_{\rm CW}^{48}$ to the $b_{\rm IV}$ suggests it may serve as a useful probe of the IVSO interaction once the density dependence of symmetry energy is well constrained.

Our study establishes a consistent relativistic framework for incorporating the IVSO mechanism and offers new insights into the isovector properties of finite nuclei and dense matter. The pivotal role of the IVSO interaction highlighted here calls for future high-precision PVES experiments to further constrain the neutron distribution, symmetry energy and the IVSO interaction.

Acknowledgments.— ZZ would like to thank Qiang Zhao and Peng-Wei Zhao for helpful discussions on the covariant DDPC density functional. This work was supported in part by the National Natural Science Foundation of China under Grant Nos. 12235010, 12575137 and 12147101, the National SKA Program of China No. 2020SKA0120300, the Science and Technology Commission of Shanghai Municipality under Grant No. 23JC1402700.

- * Corresponding author:zhangzh275@mail.sysu.edu.cn
 † Corresponding author:lwchen@sjtu.edu.cn
- [1] B. A. Brown, Neutron radii in nuclei and the neutron equation of state, Phys. Rev. Lett. **85**, 5296 (2000).
- [2] S. Typel and B. A. Brown, Neutron radii and the neutron equation of state in relativistic models, Phys. Rev. C 64, 027302 (2001).
- [3] D. Akimov et al. (COHERENT), Observation of Coherent Elastic Neutrino-Nucleus Scattering, Science 357, 1123 (2017).
- [4] M. Cadeddu, C. Giunti, Y. F. Li, and Y. Y. Zhang, Average CsI neutron density distribution from COHERENT data, Phys. Rev. Lett. 120, 072501 (2018).
- [5] X.-R. Huang, C.-L. Sun, L.-W. Chen, and J. Gao, Bayesian inference of supernova neutrino spectra with multiple detectors, JCAP 09, 040.
- [6] J. Piekarewicz, Weak-charge radius of Ar40: From CREX constraints to CEνNS sensitivity, Phys. Rev. C 112, 054312 (2025).
- [7] H. Zheng, Z. Zhang, and L.-W. Chen, Form Factor Effects in the Direct Detection of Isospin-Violating Dark Matter, JCAP 08 (011), 011.

- [8] R. J. Furnstahl, Neutron radii in mean field models, Nucl. Phys. A 706, 85 (2002).
- [9] S. Yoshida and H. Sagawa, Neutron skin thickness and equation of state in asymmetric nuclear matter, Phys. Rev. C 69, 024318 (2004).
- [10] L.-W. Chen, C. M. Ko, and B.-A. Li, Nuclear matter symmetry energy and the neutron skin thickness of heavy nuclei, Phys. Rev. C 72, 064309 (2005).
- [11] M. Centelles, X. Roca-Maza, X. Vinas, and M. Warda, Nuclear symmetry energy probed by neutron skin thickness of nuclei, Phys. Rev. Lett. 102, 122502 (2009).
- [12] L.-W. Chen, C. M. Ko, B.-A. Li, and J. Xu, Density slope of the nuclear symmetry energy from the neutron skin thickness of heavy nuclei, Phys. Rev. C 82, 024321 (2010).
- [13] P. G. Reinhard and W. Nazarewicz, Information content of a new observable: The case of the nuclear neutron skin, Phys. Rev. C 81, 051303 (2010).
- [14] X. Roca-Maza, M. Centelles, X. Vinas, and M. Warda, Neutron skin of ²⁰⁸Pb, nuclear symmetry energy, and the parity radius experiment, Phys. Rev. Lett. **106**, 252501 (2011).
- [15] B. K. Agrawal, J. N. De, and S. K. Samaddar, Determining the density content of symmetry energy and neutron skin: an empirical approach, Phys. Rev. Lett. 109, 262501 (2012).
- [16] Z. Zhang and L.-W. Chen, Constraining the symmetry energy at subsaturation densities using isotope binding energy difference and neutron skin thickness, Phys. Lett. B 726, 234 (2013).
- [17] C. Mondal, B. K. Agrawal, M. Centelles, G. Colò, X. Roca-Maza, N. Paar, X. Viñas, S. K. Singh, and S. K. Patra, Model dependence of the neutron-skin thickness on the symmetry energy, Phys. Rev. C 93, 064303 (2016).
- [18] A. R. Raduta and F. Gulminelli, Nuclear skin and the curvature of the symmetry energy, Phys. Rev. C 97, 064309 (2018).
- [19] M. Thiel, C. Sfienti, J. Piekarewicz, C. J. Horowitz, and M. Vanderhaeghen, Neutron skins of atomic nuclei: per aspera ad astra, J. Phys. G 46, 093003 (2019).
- [20] W. G. Newton and G. Crocombe, Nuclear symmetry energy from neutron skins and pure neutron matter in a Bayesian framework, Phys. Rev. C 103, 064323 (2021).
- [21] P.-G. Reinhard, X. Roca-Maza, and W. Nazarewicz, Information Content of the Parity-Violating Asymmetry in Pb208, Phys. Rev. Lett. 127, 232501 (2021).
- [22] W. G. Lynch and M. B. Tsang, Decoding the density dependence of the nuclear symmetry energy, Phys. Lett. B 830, 137098 (2022).
- [23] A. W. Steiner, M. Prakash, J. M. Lattimer, and P. J. Ellis, Isospin asymmetry in nuclei and neutron stars, Phys. Rep. 411, 325 (2005).
- [24] V. Baran, M. Colonna, V. Greco, and M. Di Toro, Reaction dynamics with exotic nuclei, Phys. Rep. 410, 335 (2005).
- [25] J. M. Lattimer and M. Prakash, Neutron Star Observations: Prognosis for Equation of State Constraints, Phys. Rept. 442, 109 (2007).
- [26] B. A. Li, L. W. Chen, and C. M. Ko, Recent progress and new challenges in isospin physics with heavy-ion reactions, Phys. Rep. 464, 113 (2008).
- [27] C. J. Horowitz, E. F. Brown, Y. Kim, W. G. Lynch, R. Michaels, A. Ono, J. Piekarewicz, M. B. Tsang, and H. H. Wolter, A way forward in the study of the symme-

- try energy: experiment, theory, and observation, J. Phys. G 41, 093001 (2014).
- [28] S. Gandolfi, A. Gezerlis, and J. Carlson, Neutron Matter from Low to High Density, Ann. Rev. Nucl. Part. Sci. 65, 303 (2015).
- [29] F. Özel and P. Freire, Masses, Radii, and the Equation of State of Neutron Stars, Ann. Rev. Astron. Astrophys. 54, 401 (2016).
- [30] M. Baldo and G. F. Burgio, The nuclear symmetry energy, Prog. Part. Nucl. Phys. 91, 203 (2016).
- [31] X. Roca-Maza and N. Paar, Nuclear equation of state from ground and collective excited state properties of nuclei, Prog. Part. Nucl. Phys. 101, 96 (2018).
- [32] C. Drischler, J. W. Holt, and C. Wellenhofer, Chiral Effective Field Theory and the High-Density Nuclear Equation of State, Ann. Rev. Nucl. Part. Sci. 71, 403 (2021).
- [33] B.-A. Li, B.-J. Cai, W.-J. Xie, and N.-B. Zhang, Progress in Constraining Nuclear Symmetry Energy Using Neutron Star Observables Since GW170817, Universe 7, 182 (2021).
- [34] J. M. Mammei, C. J. Horowitz, J. Piekarewicz, B. Reed, and C. Sfienti, Neutron Skins: Weak Elastic Scattering and Neutron Stars, Annu. Rev. Nucl. Part. Sci. 10.1146/annurev-nucl-102122-024207 (2023).
- [35] D. Adhikari et al. (PREX), Accurate Determination of the Neutron Skin Thickness of ²⁰⁸Pb through Parity-Violation in Electron Scattering, Phys. Rev. Lett. 126, 172502 (2021).
- [36] D. Adhikari et al. (CREX), Precision Determination of the Neutral Weak Form Factor of Ca48, Phys. Rev. Lett. 129, 042501 (2022).
- [37] B. T. Reed, F. J. Fattoyev, C. J. Horowitz, and J. Piekarewicz, Implications of PREX-2 on the Equation of State of Neutron-Rich Matter, Phys. Rev. Lett. 126, 172503 (2021).
- [38] P.-G. Reinhard, X. Roca-Maza, and W. Nazarewicz, Combined Theoretical Analysis of the Parity-Violating Asymmetry for Ca48 and Pb208, Phys. Rev. Lett. 129, 232501 (2022).
- [39] Z. Zhang and L.-W. Chen, Bayesian inference of the symmetry energy and the neutron skin in Ca48 and Pb208 from CREX and PREX-2, Phys. Rev. C 108, 024317 (2023).
- [40] E. Yüksel and N. Paar, Implications of parity-violating electron scattering experiments on 48Ca (CREX) and 208Pb (PREX-II) for nuclear energy density functionals, Phys. Lett. B 836, 137622 (2023).
- [41] T. Miyatsu, M.-K. Cheoun, K. Kim, and K. Saito, Can the PREX-2 and CREX results be understood by relativistic mean-field models with the astrophysical constraints?, Phys. Lett. B 843, 138013 (2023).
- [42] M. Kumar, S. Kumar, V. Thakur, R. Kumar, B. K. Agrawal, and S. K. Dhiman, CREX- and PREX-IImotivated relativistic interactions and their implications for the bulk properties of nuclear matter and neutron stars, Phys. Rev. C 107, 055801 (2023).
- [43] C. Mondal and F. Gulminelli, Nucleonic metamodeling in light of multimessenger, PREX-II, and CREX data, Phys. Rev. C 107, 015801 (2023).
- [44] S. Yang, R. Li, and C. Xu, α clustering in nuclei and its impact on the nuclear symmetry energy, Phys. Rev. C 108, L021303 (2023).
- [45] B. T. Reed, F. J. Fattoyev, C. J. Horowitz, and

- J. Piekarewicz, Density dependence of the symmetry energy in the post–PREX-CREX era, Phys. Rev. C **109**, 035803 (2024).
- [46] M. Salinas and J. Piekarewicz, Impact of tensor couplings with scalar mixing on covariant energy density functionals, Phys. Rev. C 109, 045807 (2024).
- [47] X. Roca-Maza and D. H. Jakubassa-Amundsen, QED Corrections to the Parity-Violating Asymmetry in High-Energy Electron-Nucleus Collisions, Phys. Rev. Lett. 134, 192501 (2025).
- [48] T.-G. Yue, Z. Zhang, and L.-W. Chen, PREX and CREX: Evidence for Strong Isovector Spin-Orbit Interaction, arXiv:2406.03844 [nucl-th] (2024).
- [49] T. Zhao, Z. Lin, B. Kumar, A. W. Steiner, and M. Prakash, Characterizing the nuclear models informed by PREX and CREX: a view from Bayesian inference, arXiv:2406.05267 [nucl-th] (2024).
- [50] A. Kunjipurayil, J. Piekarewicz, and M. Salinas, Role of the isovector spin-orbit potential in mitigating the CREX-PREX dilemma, Phys. Rev. C 112, 014310 (2025).
- [51] R. J. Furnstahl, J. J. Rusnak, and B. D. Serot, The Nuclear spin orbit force in chiral effective field theories, Nucl. Phys. A 632, 607 (1998).
- [52] W. Z. Jiang, Y. L. Zhao, Z. Y. Zhu, and S. F. Shen, Role of rhoNN tensor coupling and 2s (1/2) occupation in light exotic nuclei, Phys. Rev. C 72, 024313 (2005).
- [53] A. Sulaksono, T. J. Burvenich, P. O. Hess, and J. A. Maruhn, Nonrelativistic limit of point-coupling model, Int. J. Mod. Phys. E 20, 139 (2011).
- [54] T. Niksic, D. Vretenar, and P. Ring, Relativistic Nuclear Energy Density Functionals: Adjusting parameters to binding energies, Phys. Rev. C 78, 034318 (2008).
- [55] Q. Zhao, Z. Ren, P. Zhao, and J. Meng, Covariant density functional theory with localized exchange terms, Phys. Rev. C 106, 034315 (2022).
- [56] S. Typel and H. H. Wolter, Relativistic mean field calculations with density dependent meson nucleon coupling, Nucl. Phys. A 656, 331 (1999).
- [57] C. J. Horowitz and J. Piekarewicz, Impact of spin-orbit currents on the electroweak skin of neutron-rich nuclei, Phys. Rev. C 86, 045503 (2012).
- [58] P. Klupfel, P. G. Reinhard, T. J. Burvenich, and J. A. Maruhn, Variations on a theme by Skyrme: A systematic study of adjustments of model parameters, Phys. Rev. C 79, 034310 (2009).
- [59] N. Schwierz, I. Wiedenhover, and A. Volya, Parameterization of the Woods-Saxon Potential for Shell-Model Calculations, arXiv:0709.3525 [nucl-th] (2007), arXiv:0709.3525.
- [60] M. Qiu, B.-J. Cai, L.-W. Chen, C.-X. Yuan, and Z. Zhang, Bayesian model averaging for nuclear symmetry energy from effective proton-neutron chemical potential difference of neutron-rich nuclei, Phys. Lett. B 849, 138435 (2024).
- [61] R. Machleidt and F. Sammarruca, Recent advances in chiral EFT based nuclear forces and their applications, Prog. Part. Nucl. Phys. 137, 104117 (2024).
- [62] T.-G. Yue, L.-W. Chen, Z. Zhang, and Y. Zhou, Constraints on the symmetry energy from PREX-II in the multimessenger era, Phys. Rev. Res. 4, L022054 (2022).
- [63] M. Kumar, S. Kumar, Queena, R. Kumar, and S. K. Dhiman, Trends of nuclear matter and neutron-star observables post CREX-PREX-II results within the relativistic

mean field model, Phys. Rev. C 110, 055802 (2024). [64] H. De Vries, C. De Jager, and C. De Vries, Nuclear charge-density-distribution parameters from elastic electron scattering, Atomic Data and Nuclear Data Tables ${f 36},\,495$ (1987).

Supplemental Material for "Resolving the PREX-CREX puzzle in covariant density functional theory"

Mengying Qiu, ¹ Tong-Gang Yue, ² Zhen Zhang, ^{1,3,*} and Lie-Wen Chen^{2,†}

¹Sino-French Institute of Nuclear Engineering and Technology, Sun Yat-Sen University, Zhuhai 519082, China ²State Key Laboratory of Dark Matter Physics, Key Laboratory for Particle Astrophysics and Cosmology (MOE), and Shanghai Key Laboratory for Particle Physics and Cosmology,

School of Physics and Astronomy, Shanghai Jiao Tong University, Shanghai, 200240, China

³Shanghai Research Center for Theoretical Nuclear Physics,

NSFC and Fudan University, Shanghai, 200438, China

This Supplemental Material provides additional details supporting the main text. Section S.I describes the calculations of charge and weak-charge form factors. Section S.II outlines the fitting procedure used to construct the three new covariant energy density functionals (EDFs), ZH-1, ZH-2, and ZH-3. Section S.III presents the performance of these EDFs, including ground-state properties of representative nuclei and the neutron matter equation of state. Section S.IV details the nonrelativistic reduction and the resulting spin-orbit interaction. Finally, Section S.V examines the correlation of the neutron skin thickness and the charge-weak form factor difference with the density dependence of the symmetry energy.

S.I. Calculations of Charge and Weak-Charge Form Factors

In the framework of covariant energy density functionals (EDFs), the charge and weak-charge form factors are calculated following the prescription of Ref. [1], where contributions from both the vector densities and tensor currents are explicitly included. Within the impulse approximation, the charge form factors $F_{\rm C}$ and weak-charge form factors $F_{\rm W}$, both normalized to one at q=0, are given by:

$$F_{\mathrm{C}}(q) = \frac{e^{a_{\mathrm{cm}}q^{2}}}{Z} \sum_{i=p,n} \left\{ G_{\mathrm{E}}^{i}\left(q^{2}\right) F_{\mathrm{V}}^{i}(q) + \left(\frac{G_{\mathrm{M}}^{i}\left(q^{2}\right) - G_{\mathrm{E}}^{i}\left(q^{2}\right)}{1+\lambda}\right) \times \left[\lambda F_{\mathrm{V}}^{i}(q) + \frac{q}{2m} F_{\mathrm{T}}^{i}(q)\right] \right\},$$

$$F_{\mathrm{W}}(q) = \frac{e^{a_{\mathrm{cm}}q^{2}}}{Zg_{\mathrm{V}}^{\mathrm{p}} + Ng_{\mathrm{V}}^{\mathrm{n}}} \sum_{i=n,n} \left\{ \widetilde{G}_{\mathrm{E}}^{i}\left(q^{2}\right) F_{\mathrm{V}}^{i}(q) + \left(\frac{\widetilde{G}_{\mathrm{M}}^{i}\left(q^{2}\right) - \widetilde{G}_{\mathrm{E}}^{i}\left(q^{2}\right)}{1+\lambda}\right) \times \left[\lambda F_{\mathrm{V}}^{i}(q) + \frac{q}{2m} F_{\mathrm{T}}^{i}(q)\right] \right\},$$
(S1)

where $\lambda = q^2/(4m)$, and $a_{\rm cm} = \hbar^2/\left(8\langle\hat{P}_{\rm c.m.}^2\rangle\right)$ accounts for the center-of-mass correction. $G_{\rm E,M}^i$ are the intrinsic nucleon electromagnetic form factors, and $\widetilde{G}_{\rm E,M}^i$ are the weak intrinsic nucleon form form factors. $g_{\rm v}^n$ and $g_{\rm v}^p$ are radiatively corrected weak-vector charges of the neutron and proton, respectively.

Under spherical symmetry, the single-particle solution of Dirac equation takes the form

$$\psi_{n\kappa m}(\mathbf{r}) = \frac{1}{r} \begin{pmatrix} g_{n\kappa}(r) \mathcal{Y}_{+\kappa m}(\hat{\mathbf{r}}) \\ i f_{n\kappa}(r) \mathcal{Y}_{-\kappa m}(\hat{\mathbf{r}}) \end{pmatrix}$$
(S2)

where n, κ , m are the principal, Dirac and magnetic quantum numbers, respectively, and $\mathcal{Y}(\hat{\mathbf{r}})$ are the spin-spherical harmonics. The vector and tensor form factors are then expressed as

$$F_{V}(q) = \int \bar{\psi}(\mathbf{r})e^{i\mathbf{q}\cdot\mathbf{r}}\gamma^{0}\psi(\mathbf{r})d^{3}r$$

$$= \sum_{n\kappa} (2j+1) \int_{0}^{\infty} \left[g_{n\kappa}^{2}(r) + f_{n\kappa}^{2}(r)\right] j_{0}(qr)dr,$$

$$F_{T}(q) = \int \bar{\psi}(\mathbf{r})e^{i\mathbf{q}\cdot\mathbf{r}}\gamma^{0}\gamma \cdot \hat{\mathbf{q}}\psi(\mathbf{r})d^{3}r$$

$$= \sum_{n\kappa} 2(2j+1) \int_{0}^{\infty} g_{n\kappa}(r)f_{n\kappa}(r)j_{1}(qr)dr,$$
(S3)

^{*} Corresponding author:zhangzh275@mail.sysu.edu.cn

[†] Corresponding author:lwchen@sjtu.edu.cn

where $j_l(qr)$ are spherical Bessel functions.

For intrinsic single-nucleon electromagnetic form factors, a simple dipole parametrization is adopted, which provides a good approximation at moderate momentum transfers. Specifically,

$$G_{\rm E}^{p}\left(q^{2}\right) = \frac{G_{\rm M}^{p}\left(q^{2}\right)}{\mu_{p}} = \frac{G_{\rm M}^{n}\left(q^{2}\right)}{\mu_{n}} = G_{\rm D}\left(q^{2}\right),$$
 (S4)

where the dipole form factor is given by

$$G_{\rm D}\left(q^2\right) = \left(1 + \frac{q^2}{12}r_p^2\right)^{-2}.$$
 (S5)

The proton mean-square radius r_p^2 , as well as the magnetic moments μ_p and μ_n are listed in Table S1. For the neutron electromagnetic form factor, we adopt the Galster parametrization

$$G_{\rm E}^n(q^2) = -\left(\frac{q^2 r_n^2 / 6}{1 + q^2 / m^2}\right) G_{\rm D}(q^2),$$
 (S6)

where r_n^2 is the neutron mean-square radius.

As for weak intrinsic nucleon form factors, they can be expressed as the sum of the corresponding electromagnetic form factors, weighted by the nucleonic weak charges $g_{\mathbf{v}}^{i}$, together with a strange quark contribution, i.e.,

$$\widetilde{G}_{E,M}^{p}\left(q^{2}\right) = g_{v}^{p} G_{E,M}^{p}\left(q^{2}\right) + g_{v}^{n} G_{E,M}^{n}\left(q^{2}\right) + \xi_{v}^{(0)} G_{E,M}^{s}\left(q^{2}\right),
\widetilde{G}_{E,M}^{n}\left(q^{2}\right) = g_{v}^{n} G_{E,M}^{p}\left(q^{2}\right) + g_{v}^{p} G_{E,M}^{n}\left(q^{2}\right) + \xi_{v}^{(0)} G_{E,M}^{s}\left(q^{2}\right),$$
(S7)

where $\xi_{\rm v}^{(0)}$ is the *singlet* weak charge. For the strange quark electric form factor $G_{\rm E}^s$, we follow the parametrization of Ref. [2] and adopt

$$G_{\rm E}^s(q^2) = \rho_s \frac{q^2/(4m^2)}{1 + 4.97q^2/(4m^2)},$$
 (S8)

where ρ_s the strange quark electric coupling. For the strange quark magnetic form factor, which should equal strange magnetic moment κ_s at $q^2 = 0$ [1], we adopt the following dipole-like parametrization

$$G_{\mathcal{M}}^{s}\left(q^{2}\right) = \frac{\kappa_{s}}{\left(1 + \frac{q^{2}}{12\kappa_{s}}r_{\mathcal{M},s}^{2}\right)^{2}}.$$
(S9)

where $r_{M,s}^2$ is the strange magnetic radius. All parameters entering in the calculations of the charge and weak charge form factors are listed in Table S1.

TABLE S1. Parameters used in the calculation of charge and weak-charge form factors, including the radiatively corrected neutron and proton weak charges $(g_{\rm v}^{\rm n}, g_{\rm v}^{\rm p})$, nucleon mean-square radii (r_p^2, r_n^2) , magnetic dipole moments (μ_p, μ_n) , the singlet weak charge $\xi_{\rm v}^{(0)}$, the strange electric coupling ρ_s , the strange magnetic moment κ_s , and the strange magnetic radius $r_{\rm M,s}^2$.

parameters	values	Ref
$g_{ m v}^{ m p}$	0.0721	[1]
$g_{ m v}^{ m n}$	-0.9878	[1]
$r_p^2 [\mathrm{fm}^2]$	0.6906	[3]
$r_n^2 [\mathrm{fm}^2]$	-0.116	[4]
μ_p	2.793	[1]
μ_n	-1.913	[1]
$\xi_{ m v}^{(0)}$	-0.9877	[1]
$ ho_s$	-0.24	[2]
κ_s	-0.017	[2]
$r_{ m M,s}^2~{ m [fm^2]}$	-0.015	[5]
·		

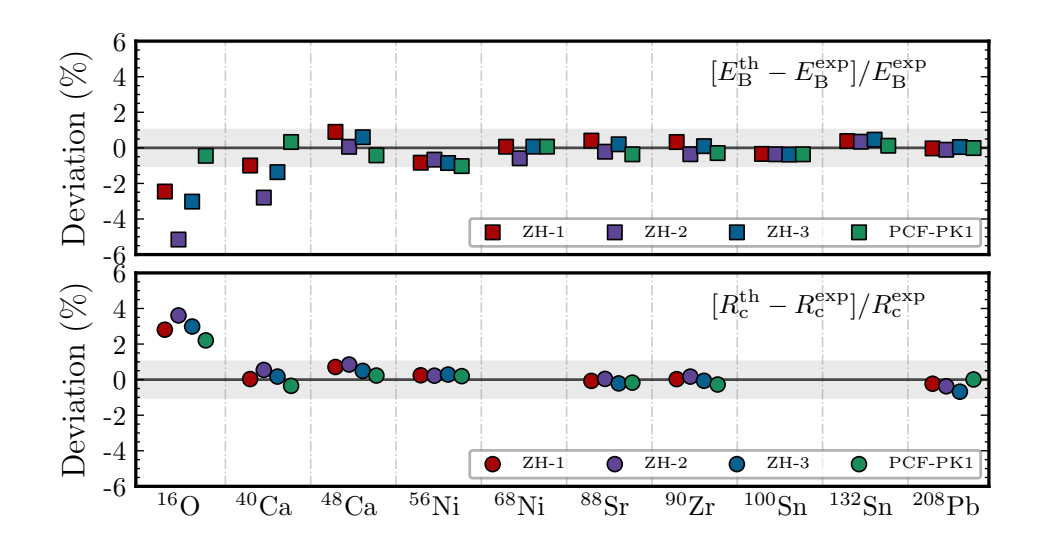


FIG. S1. Relative deviations of binding energies $E_{\rm B}$ (open squares) and charge radii $R_{\rm c}$ (open circles) of 16 O, 40 Ca, 48 Ca, 56 Ni, 68 Ni, 88 Sr, 90 Zr, 100 Sn, 132 Sn, and 208 Pb, calculated using the ZH-1, ZH-2, and ZH-3, relative to experimental measurements [6, 13–15]. The shaded band represents $\pm 1\%$ relative deviation.

S.II. Fitting protocol and dataset

In addition to the charge-weak form factor differences in 48 Ca and 208 Pb, the fitting protocol incorporates a selected set of experimental or empirical data to ensure a reasonable description of both finite nuclei and nuclear matter. Specifically, the nuclear ground-state data include the binding energies $E_{\rm B}$, charge radii $R_{\rm C}$ of 48 Ca and 208 Pb, and spin-orbit (SO) splittings $\Delta\epsilon_{\rm ls}$ of the $\nu 1f$ orbital in 48 Ca and the $\pi 2d$, $\nu 3p$, and $\nu 2f$ orbitals in 208 Pb [6–8]. In the fitting protocol, we also employ the symmetry energy value at 2/3 saturation density, $E_{\rm sym}(2\rho_{\rm sat}/3) = 25.6^{+1.4}_{-1.3}$ MeV, obtained from EDF analyses of nuclear masses [9], together with the neutron matter equation of state around 1/3 saturation density, $E_{\rm PNM}(\rho=0.04805~{\rm fm}^{-3})=6.72\pm0.08$ MeV predicted by chiral effective field theory [10]. The experimental values for nuclear ground-state observables employed in the fits are summarized in Table S2.

TABLE S2. Experimental data for the ground-state properties of ⁴⁸Ca and ²⁰⁸Pb used in the fitting protocol, including the binding energies $E_{\rm B}$ [6], charge radii $R_{\rm C}$ [6], spin-orbit splittings $\Delta \epsilon_{\rm ls}$ [7], and charge-weak form factor differences $\Delta F_{\rm CW}$ [11, 12].

Nucleus	$E_{\rm B} \ [{ m MeV}] \ [6]$	$R_{\rm C}$ [fm] [6]	$\Delta \epsilon_{\mathrm{ls}} \; [\mathrm{MeV}] \; [7]$	$\Delta F_{\rm CW}$ [11, 12]
$^{48}\mathrm{Ca}$	-415.990	3.477	$8.80 \ (\nu 1f)$	0.0277 ± 0.0055
			$1.46 \; (\pi 2d)$	
$^{208}\mathrm{Pb}$	-1636.446	5.501	$0.89 \ (\nu 3p)$	0.041 ± 0.013
			$2.13 \; (\nu 2f)$	

Based on the selected dataset, we perform the Emcee sampling [16] in the parameter space according to the log-likelihood function

$$\log \mathcal{L} = -\sum_{i} \log \sigma_{i} - \frac{1}{2} \sum_{i} \frac{\left[\mathcal{O}_{i}^{\exp} - \mathcal{O}_{i}(\boldsymbol{\theta})\right]^{2}}{\sigma_{i}^{2}}, \tag{S10}$$

where $\mathcal{O}_i^{\text{exp}}$ denotes the experimental data, $\mathcal{O}_i(\boldsymbol{\theta})$ the theoretical predictions at parameter set $\boldsymbol{\theta}$, and σ_i the adopted error for each type of observable. The σ_i for binding energies, charge radii, and SO splittings are treated as free sampling parameters, whereas those of the charge-weak form factor differences are fixed to their experimental values.

From the full ensemble of samples, three new parametrizations are selected according to the following criteria: (1) they simultaneously reproduce the charge-weak form factor differences measured by CREX and PREX-II within their 1σ uncertainties; (2) the density slope of symmetry energy at saturation density $L(\rho_{\rm sat})$ lies in the range of 10-100 MeV; (3) The binding energies of 16 O, 40 Ca, 48 Ca, 56 Ni, 88 Sr, 90 Zr, 100 Sn, 132 Sn, 208 Pb, and charge radii of

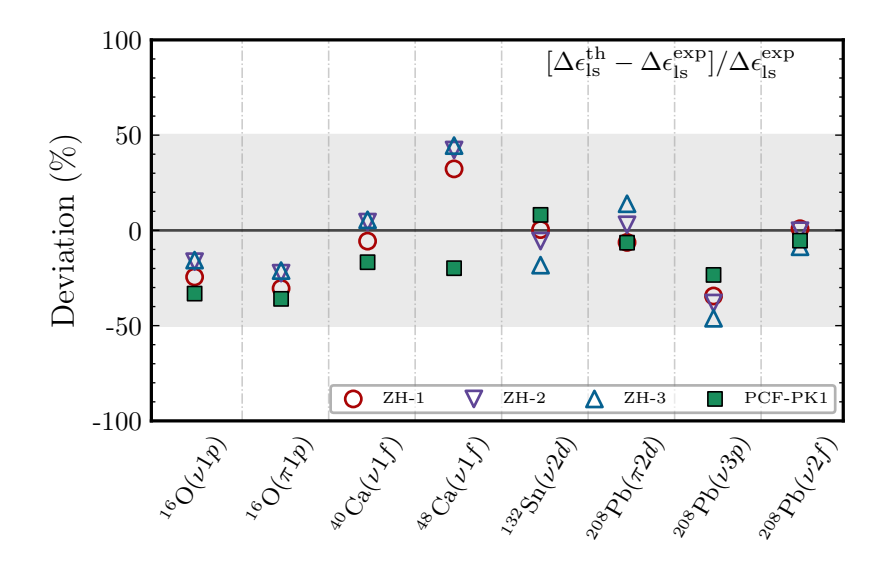


FIG. S2. Relative deviations of SO splitting energies $\Delta \epsilon_{ls}$ in 16 O, 40,48 Ca, 132 Sn, and 208 Pb, calculated using the ZH-1, ZH-2, ZH-3 and PCF-PK1, relative to experimental measurements [7, 8]. The shaded band represents $\pm 50\%$ relative deviation.

 16 O, 40 Ca, 48 Ca, 56 Ni, 88 Sr, 90 Zr, 208 Pb, are reproduced within approximately 1%; and (4) if several parameter sets satisfy all constraints equally well, the one with the smallest total relative deviation from experimental data is chosen. Finally, three parametrizations exhibiting distinct values of $L(\rho_{\text{sat}})$ are chosen as the representative ZH family.

S.III. Performance of the new EDFs

We begin by examining the performance of the three new EDFs for global properties of finite nuclei. Figure. S1 shows the relative deviations of the binding energies $E_{\rm B}$ and charge radii $R_{\rm C}$ from experimental data [6, 13–15] for 10 typical doubly-magic and semi-magic nuclei. To account for the non-negligible finite nucleon size effects and intrinsic electromagnetic structure corrections [17], the charge radii are computed from the corresponding charge form factor at zero momentum transfer as

$$R_{\rm C} = \sqrt{-\frac{6}{F_{\rm C}(0)} \frac{dF_{\rm C}(q)}{dq^2} \Big|_{q=0}},$$
 (S11)

with the factor $F_{\rm C}(0)$ ensuring the proper normalization to the total nuclear charge. Although only properties of ⁴⁸Ca and ²⁰⁸Pb were considered in the fitting protocol, the new EDFs provides reasonable descriptions across the ten nuclei. The relative deviations generally lie in 1%, except for the light nuclei ¹⁶O and ⁴⁰Ca. Figure S2 shows the relative deviations of the SO splittings $\Delta\epsilon_{\rm ls}$ in ¹⁶O, ^{40,48}Ca, ¹³²Sn, and ²⁰⁸Pb with respect to experimental values [7, 8]. As seen, the present ZH family overall reproduce the experimental SO splittings within 50% relative deviation.

Recently, Ref. [19] has suggested that an excessively strong IVSO potential may lead to a level crossing between the neutron l=6 spin-orbit partners in 208 Pb, thereby destroying the N=126 shell closure. We show in Figs. S3 and S4 the single-particle energies predicted by the ZH family and PCF-PK1 for 48 Ca and 208 Pb, respectively. It is seen that, despite the enhanced IVSO strength in the ZH family, the obtained ordering of the SO partners remains correct near the Fermi surface, and the shell closures are well preserved.

Finally, we examine the description for nuclear matter. Figure S5 shows the pure neutron matter equation of state E_{PNM} as a function of neutron density ρ_n . Also shown in Fig. S5 are predictions from chiral effective field theory (χEFT) calculations [10, 18]. As demonstrated, all three new predictions are in good agreement with the microscopic predictions [10, 18].

S.IV. Nonrelativistic reduction and the spin-orbit couplings

Neglecting the kinetic, Coulomb and pairing contributions, the energy density of the nuclear system is given by

$$\mathcal{E} = \frac{1}{2} \alpha_{\rm S} \rho_{\rm S}^2 + \frac{1}{2} \alpha_{\rm V} \rho_{\rm V}^2 + \frac{1}{2} \alpha_{\tau \rm S} \rho_{\tau \rm S}^2 + \frac{1}{2} \alpha_{\tau \rm V} \rho_{\tau \rm V}^2 - \alpha_{\tau \rm T} \mathbf{j}_{\tau \rm T}^{0}^2 - \alpha_{\rm T} \mathbf{j}_{\rm T}^{0}^2 - \frac{1}{2} \delta_{\rm S} \left(\nabla \rho_{\rm S} \right)^2, \tag{S12}$$

where

$$\rho_{S} = \rho_{S,n} + \rho_{S,p}, \qquad \rho_{\tau S} = \rho_{S,n} - \rho_{S,p},
\rho_{V} = \rho_{V,n} + \rho_{V,p}, \qquad \rho_{\tau V} = \rho_{V,n} - \rho_{V,p},
\mathbf{j}_{T}^{0} = \mathbf{j}_{T,n}^{0} + \mathbf{j}_{T,p}^{0}, \qquad \mathbf{j}_{\tau T}^{0} = \mathbf{j}_{T,n}^{0} - \mathbf{j}_{T,p}^{0}.$$
(S13)

The nucleon scalar, vector and tensor densities are defined as

$$\rho_{S,q} = \sum_{\alpha} \bar{\psi}_{\alpha} \psi_{\alpha} = \sum_{\alpha} \left[\varphi_{\alpha}^{\dagger} \varphi_{\alpha} - \chi_{\alpha}^{\dagger} \chi_{\alpha} \right]
\rho_{V,q} = \sum_{\alpha} \bar{\psi}_{\alpha} \gamma^{0} \psi_{\alpha} = \sum_{\alpha} \left[\varphi_{\alpha}^{\dagger} \varphi_{\alpha} + \chi_{\alpha}^{\dagger} \chi_{\alpha} \right]
\mathbf{j}_{T,q}^{0} = \sum_{\alpha} \bar{\psi}_{\alpha} i \gamma^{0} \gamma \psi_{\alpha} = \sum_{\alpha} \left[\varphi_{\alpha}^{\dagger} i \boldsymbol{\sigma} \chi_{\alpha} - \chi_{\alpha}^{\dagger} i \boldsymbol{\sigma} \varphi_{\alpha} \right]$$
(S14)

where q = p, n, and $\psi_{\alpha} = (\varphi_{\alpha}, \chi_{\alpha})^{\mathrm{T}}$ is the Dirac four-spinor of the occupied single-particle state α for nucleon species q, with φ_{α} and χ_{α} denoting its upper and lower components, respectively.

To reveal the implicit spin-orbit interaction, we perform a nonrelativistic reduction and reexpress the \mathcal{E} in terms of standard nonrelativistic densities and currents built from the normalized *classical* wave function ϕ^{cl} [20–22]:

$$\rho_{q} = \sum_{\alpha} |\phi_{\alpha}^{\text{cl}}|^{2}, \qquad \tau_{q} = \sum_{\alpha} |\nabla \phi_{\alpha}^{\text{cl}}|^{2},$$

$$J_{q} = -\frac{i}{2} \sum_{\alpha} \left[\phi_{\alpha}^{\text{cl}\dagger} (\nabla \times \boldsymbol{\sigma}) \phi_{\alpha}^{\text{cl}} - (\nabla \times \boldsymbol{\sigma} \phi_{\alpha}^{\text{cl}})^{\dagger} \phi_{\alpha}^{\text{cl}} \right],$$
(S15)

where ρ_q , τ_q , and J_q are nucleon number density, kinetic energy density and SO density, respectively.

To proceed, we eliminate the lower component of the Dirac four-spinor. For simplification of notation, we omit the state index α in what follows. Variation of the Lagrangian density yields the single-nucleon Dirac equation

$$\left[\boldsymbol{\alpha} \cdot \boldsymbol{p} + \beta(m + S_q) + V_q^0 - i\beta\boldsymbol{\alpha} \cdot \boldsymbol{T}_q^0\right] \psi = \epsilon_q \psi, \tag{S16}$$

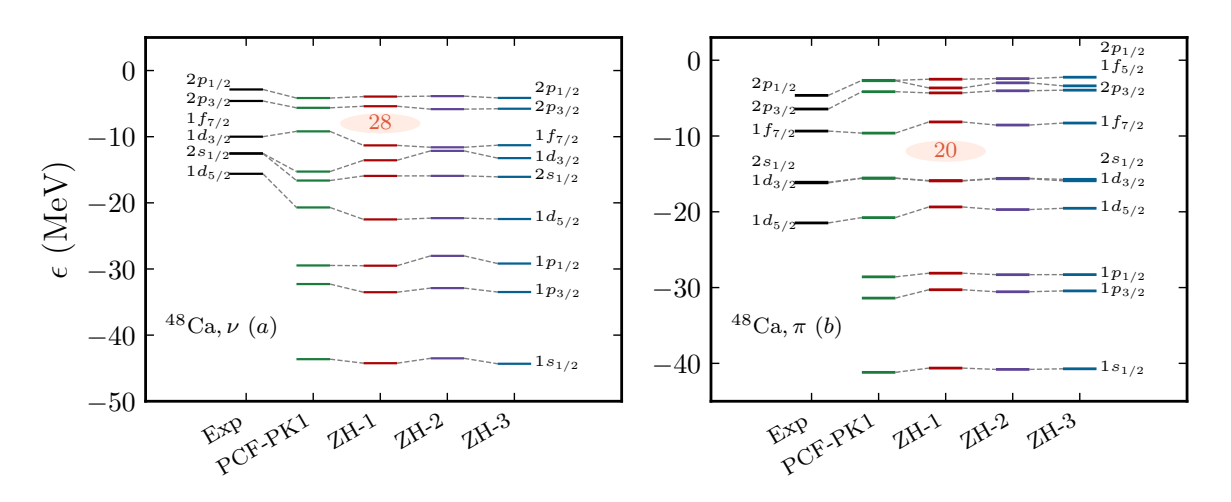


FIG. S3. Neutron (a) and proton (b) single particle energies of ⁴⁸Ca predicted by PCF-PK1, ZH-1, ZH-2, and ZH-3. Experimental data are taken from Ref. [7].

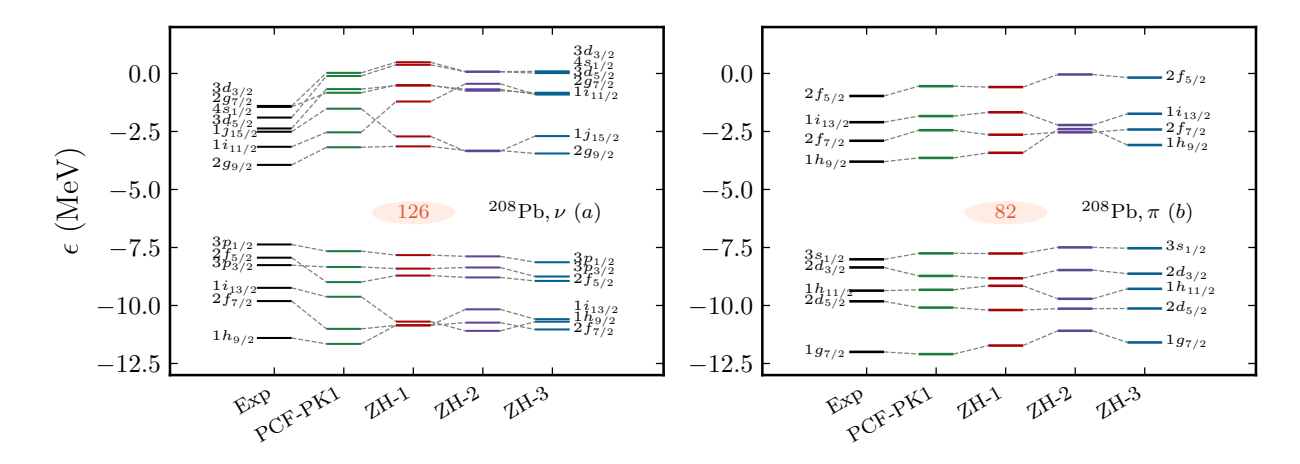


FIG. S4. Same as Figure S3, but for ²⁰⁸Pb.

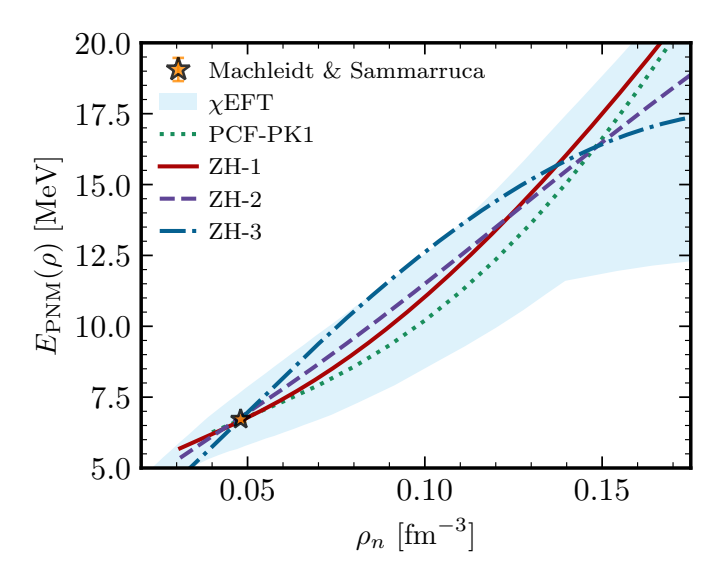


FIG. S5. The pure neutron matter equations of state as functions of neutron density ρ_n are shown for ZH-1 (red solid), ZH-2 (purple dashed), and ZH-3 (blue dash-dotted lines). For comparison, PCF-PK1 is plotted as a green dotted line, and the combined χ EFT prediction from various many-body calculations [18] is given by a blue shaded band. Chiral EFT calculation at N³LO ($E_{\rm PNM}(\rho=0.04805~{\rm fm}^{-3})=6.72\pm0.08~{\rm MeV})$ by Machleidt & Sammarruca [10] is marked by an orange star.

where the scalar, vector and tensor potentials are defined as

$$S_{q} = \alpha_{S}\rho_{S} + \tau_{3}\alpha_{\tau S}\rho_{\tau S} + \delta_{S}\Delta\rho_{S},$$

$$V_{q}^{0} = \alpha_{V}\rho_{V} + \tau_{3}\alpha_{\tau V}\rho_{\tau V} + e^{\frac{1-\tau_{3}}{2}}A^{0} + \Sigma^{r},$$

$$T_{q}^{0} = 2\alpha_{T}\mathbf{j}_{T}^{0} + 2\tau_{3}\alpha_{\tau T}\mathbf{j}_{\tau T}^{0},$$
(S17)

with $\tau_3 = 1$ and -1 for neutrons and protons, respectively. The rearrangement term Σ^r is given by

$$\Sigma^{r} = \frac{1}{2} \left(\frac{\partial \alpha_{V}}{\partial \rho_{V}} \rho_{V}^{2} + \frac{\partial \alpha_{S}}{\partial \rho_{V}} \rho_{S}^{2} + \frac{\partial \alpha_{\tau S}}{\partial \rho_{V}} \rho_{\tau S}^{2} + \frac{\partial \alpha_{\tau V}}{\partial \rho_{V}} \rho_{\tau V}^{2} \right) - \frac{\partial \alpha_{T}}{\partial \rho_{V}} \mathbf{j}_{T}^{2} - \frac{\partial \alpha_{\tau T}}{\partial \rho_{V}} \mathbf{j}_{\tau T}^{2}.$$
 (S18)

In Dirac-Pauli representation, the single-nucleon Dirac equation takes the matrix form

$$\begin{pmatrix} m+S+V^0 & \boldsymbol{\sigma} \cdot (\boldsymbol{p}-i\boldsymbol{T}^0) \\ \boldsymbol{\sigma} \cdot (\boldsymbol{p}+i\boldsymbol{T}^0) & -m-S+V^0 \end{pmatrix} \begin{pmatrix} \varphi \\ \chi \end{pmatrix} = \epsilon \begin{pmatrix} \varphi \\ \chi \end{pmatrix}.$$
 (S19)

From the second row in Eq. (S19), one obtains

$$\chi = \frac{\boldsymbol{\sigma} \cdot (\boldsymbol{p} + i\boldsymbol{T}^0)}{\epsilon + m + S_q - V_q^0} \varphi \equiv \mathcal{B}\boldsymbol{\sigma} \cdot \overrightarrow{\Pi} \varphi.$$
 (S20)

with $\overrightarrow{\Pi} = \boldsymbol{p} + i\boldsymbol{T}^0$ and $\mathcal{B}_q = \left[\epsilon + m + S_q - V_q^0\right]^{-1}$.

Next, we identify the upper component φ with the *classical* wave function ϕ^{cl} . Note that the vector density ρ_{V} must satisfy the normalization condition required by Lorentz invariance, which implies

$$\int d^3 r \bar{\psi} \gamma^0 \psi = \int d^3 r \varphi^{\dagger} \hat{I} \varphi = 1 = \int d^3 r \phi^{\text{cl}\dagger} \phi^{\text{cl}}, \tag{S21}$$

where the norm kernel is

$$\hat{I} = 1 + \boldsymbol{\sigma} \cdot \overleftarrow{\Pi} \mathcal{B}^2 \boldsymbol{\sigma} \cdot \overrightarrow{\Pi}. \tag{S22}$$

This establishes the transformation between φ and $\phi^{\rm cl}$ as

$$\phi^{\text{cl}} = \hat{I}^{1/2}\varphi, \quad \varphi = \hat{I}^{-1/2}\phi^{\text{cl}}. \tag{S23}$$

Using these relations, the nonrelativistic limit is obtained by a systematic expansion in the small quantity

$$\mathcal{B}_0 = 1/(2m^*),\tag{S24}$$

where $m^* = m + \alpha_S \rho_S$ denotes the isoscalar Dirac effective mass. In this power counting, $S_q + V_q^0$, $\epsilon_q - m$, $\tau_3 \alpha_{\tau S} \rho_{\tau S}$ and $\delta_S \Delta \rho_S$ are treated as leading-order quantities, $\mathcal{O}(1)$, and thus \mathcal{B} defined in Eq. (S20) can be expanded as

$$\mathcal{B} = \frac{1}{2m^* - (S_q + V_q^0) + (\epsilon_q - m) + 2(\tau_3 \alpha_{\tau S} \rho_{\tau S} + \delta_S \Delta \rho_S)} \simeq \mathcal{B}_0 + \mathcal{O}(\mathcal{B}_0^2). \tag{S25}$$

Taylor expanding the norm operator $\hat{I}^{-1/2}$ then gives

$$\hat{I}^{-1/2} \simeq 1 - \frac{1}{2} \left(\boldsymbol{\sigma} \cdot \overleftarrow{\Pi} \, \mathcal{B}_0^2 \, \boldsymbol{\sigma} \cdot \overrightarrow{\Pi} \right) + \mathcal{O}(\mathcal{B}_0^3),$$
 (S26)

where $\overrightarrow{\Pi} = \boldsymbol{p} + i\boldsymbol{T}^0$ and $\overleftarrow{\Pi}$ acts to the left.

Substituting Eqs. (S20), (S23), and (S26) into the density definitions in Eq. (S14), and keeping terms consistently up to order \mathcal{B}_0^2 , one obtains the nonrelativistic limits

$$\rho_{\mathbf{V},q} = \rho_{q},$$

$$\rho_{\mathbf{S},q} = \sum_{\alpha} \phi_{\alpha}^{\mathrm{cl}\dagger} \hat{I}^{-1/2} \left(1 - \boldsymbol{\sigma} \cdot \overleftarrow{\boldsymbol{\Pi}} \, \mathcal{B}_{0}^{2} \, \boldsymbol{\sigma} \cdot \overrightarrow{\boldsymbol{\Pi}} \right) \hat{I}^{-1/2} \phi_{\alpha}^{\mathrm{cl}}$$

$$= \rho_{q} - 2\mathcal{B}_{0}^{2} \left[\tau_{q} - \boldsymbol{\nabla} \cdot \boldsymbol{J}_{q} - \boldsymbol{\nabla} \rho \cdot \boldsymbol{T}_{q}^{0} + 2 \, \boldsymbol{T}_{q}^{0} \cdot \boldsymbol{J}_{q} + \rho_{q} (\boldsymbol{T}_{q}^{0})^{2} \right],$$

$$\mathbf{j}_{\mathbf{T},q}^{0} = \sum_{\alpha} \left[\phi_{\alpha}^{\mathrm{cl}\dagger} \hat{I}^{-1/2} \left(i \, \boldsymbol{\sigma} \, \mathcal{B}_{0} \, \boldsymbol{\sigma} \cdot \overrightarrow{\boldsymbol{\Pi}} \right) \hat{I}^{-1/2} \phi_{\alpha}^{\mathrm{cl}} - c.c. \right]$$

$$= \mathcal{B}_{0} \, \boldsymbol{\nabla} \rho_{q} - 2\mathcal{B}_{0} \, \boldsymbol{T}_{q}^{0} \rho - 2\mathcal{B}_{0} \, \boldsymbol{J}_{q}.$$
(S27)

Replacing the relativistic densities and currents in Eq. (S12) by their nonrelativistic limits in Eq. (S27), and expanding consistently up to order \mathcal{B}_0^2 , we obtain the nonrelativistic reduction of the covariant potential energy density:

$$\mathcal{E} = \left(\frac{1}{2}\alpha_{\mathrm{S}} + \frac{1}{2}\alpha_{\mathrm{V}}\right)\rho^{2} + \left(\frac{1}{2}\alpha_{\tau\mathrm{S}} + \frac{1}{2}\alpha_{\tau\mathrm{V}}\right)\tilde{\rho}^{2} - \frac{1}{2}\delta_{\mathrm{S}}(\nabla\rho)^{2} - 2\mathcal{B}_{0}^{2}\alpha_{\mathrm{S}}\,\rho\,\tau - 2\mathcal{B}_{0}^{2}\alpha_{\tau\mathrm{S}}\,\tilde{\rho}\,\tilde{\tau}$$

$$-\alpha_{\mathrm{T}}\mathcal{B}_{0}^{2}(\nabla\rho)^{2} - \alpha_{\tau\mathrm{T}}\mathcal{B}_{0}^{2}(\nabla\tilde{\rho})^{2} - 4\alpha_{\mathrm{T}}\mathcal{B}_{0}^{2}\boldsymbol{J}^{2} - 4\alpha_{\tau\mathrm{T}}\mathcal{B}_{0}^{2}\tilde{\boldsymbol{J}}^{2} - 2\mathcal{B}_{0}^{2}\alpha_{\tau\mathrm{S}}^{\prime}\tilde{\rho}\,\nabla\rho\cdot\tilde{\boldsymbol{J}}$$

$$+ \left(-2\mathcal{B}_{0}^{2}\alpha_{\mathrm{S}}^{\prime}\rho - 2\mathcal{B}_{0}^{2}\alpha_{\mathrm{S}} + 4\mathcal{B}_{0}^{2}\alpha_{\mathrm{T}}\right)\nabla\rho\cdot\boldsymbol{J}$$

$$+ \left(-2\mathcal{B}_{0}^{2}\alpha_{\tau\mathrm{S}} + 4\mathcal{B}_{0}^{2}\alpha_{\tau\mathrm{T}}\right)\nabla\tilde{\rho}\cdot\tilde{\boldsymbol{J}},$$
(S28)

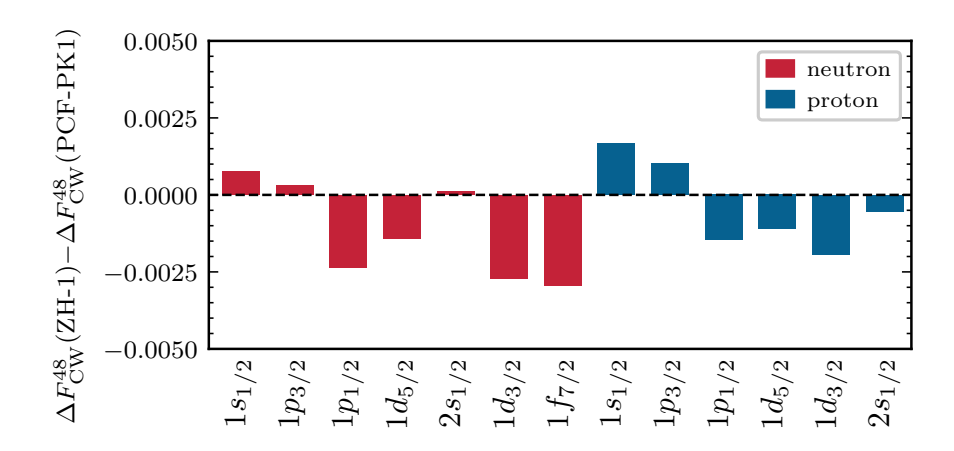


FIG. S6. Relative changes of the single-orbital contributions to the weak-charge form-factor difference $\Delta F_{\rm CW}^{48}$ in 48 Ca, obtained with ZH-1 relative to PCF-PK1. Neutron and proton orbitals are indicated in red and blue, respectively.

where $\tilde{\rho} = \rho_n - \rho_p$, $\tilde{\tau} = \tau_n - \tau_p$, and $\tilde{J} = J_n - J_p$. Primes on the couplings denote derivatives with respect to the (isoscalar) density. We note that different choices for expanding \mathcal{B} exist in the literature [20–22], but the results differ only at higher order.

By comparing Eq. (S12) with nonrelativistic Skyrme EDF [23], we identify the SO part of the functional as

$$\mathcal{E}_{SO} = \frac{b_{IS}}{2} \nabla \rho \cdot \boldsymbol{J} + \frac{b_{IV}}{2} \nabla \tilde{\rho} \cdot \tilde{\boldsymbol{J}} + \frac{b_{SV}}{2} \nabla \rho \cdot \tilde{\boldsymbol{J}}, \tag{S29}$$

where the strength parameters of the isoscalar and isovector SO interactions are

$$b_{\rm IS} = 8\mathcal{B}_0^2 \alpha_{\rm T} - 4\mathcal{B}_0^2 \alpha_{\rm S} - 4\mathcal{B}_0^2 \alpha_{\rm S}' \rho, b_{\rm IV} = 8\mathcal{B}_0^2 \alpha_{\tau \rm T} - 4\mathcal{B}_0^2 \alpha_{\tau \rm S}.$$
 (S30)

Due to the density dependence of $\alpha_{\tau S}$, an additional mixed term $\nabla \rho \cdot \tilde{J}$ appears in the nonrelativistic reduction, and we define the corresponding strength as

$$b_{\rm SV} = -4\mathcal{B}_0^2 \alpha_{\tau S}' \tilde{\rho}. \tag{S31}$$

The nonrelativistic limit of the single-particle Hamiltonian entering into the relativistic Hartree equation can be derived either through variations of Eq. (S28) or directly by a nonrelativistic reduction of the Dirac Hamiltonian as in Ref. [20]. Up to order \mathcal{B}_0^2 , both approaches lead to

$$h_q^{\text{eff}} = \boldsymbol{p}\mathcal{B}_0\boldsymbol{p} + U_q + i\boldsymbol{W}_q \cdot (\boldsymbol{\sigma} \times \boldsymbol{\nabla}), \quad q = n, p$$
 (S32)

where the effective central potential reads

$$U_{q} = (\alpha_{S} + \alpha_{V}) \rho + \tau_{3} (\alpha_{\tau S} + \alpha_{\tau V}) \tilde{\rho} + \frac{1}{2} (\alpha'_{S} + \alpha'_{S}) \rho^{2} + \frac{1}{2} (\alpha'_{\tau S} + \alpha'_{\tau S}) \tilde{\rho}^{2}$$

$$- 2\mathcal{B}_{0}^{2} \alpha_{S} \tau - 2\tau_{3} \mathcal{B}_{0}^{2} \alpha_{\tau S} \tilde{\tau} - 2\mathcal{B}_{0}^{2} \alpha'_{S} \rho \tau - 2\mathcal{B}_{0}^{2} \alpha'_{\tau S} \tilde{\rho} \tilde{\tau} + (2\mathcal{B}_{0}^{2} \alpha_{T} + \delta_{S}) \nabla^{2} \rho + 2\tau_{3} \mathcal{B}_{0}^{2} \alpha_{\tau T} \nabla^{2} \tilde{\rho}$$

$$- \frac{b_{IS}}{2} \nabla \mathbf{J} - \tau_{3} \frac{b_{IV} + \tau_{3} b_{SV}}{2} \nabla \tilde{\mathbf{J}}.$$
(S33)

The corresponding SO potential is

$$\boldsymbol{W}_{q} = \frac{b_{\mathrm{IS}} + \tau_{3} b_{\mathrm{SV}}}{2} \nabla \rho + \tau_{3} \frac{b_{\mathrm{IV}}}{2} \nabla \tilde{\rho} - 8 \mathcal{B}_{0}^{2} \alpha_{\mathrm{T}} \boldsymbol{J} - 8 \tau_{3} \mathcal{B}_{0}^{2} \alpha_{\mathrm{T}} \tilde{\boldsymbol{J}}. \tag{S34}$$

For the EDFs used in this study, the b_{SV} value is numerically small (see Tab. I in the main text), so the SO effects are dominated by the b_{IS} and b_{IV} . As Eqs. (S33) and (S34) indicate, b_{IS} and b_{IV} affects not only the spin-orbit

potential W_q but also the central mean-field U_q . To clarify which contribution primarily drives the IVSO effects on the charge-weak form factor difference $\Delta F_{\mathrm{CW}}^{48}$ in 48 Ca, we have evaluate the single-orbital contributions to the deviation between the predictions of ZH-1 and PCF-PK1. As shown in Fig. S6, the contributions from individual orbitals are relatively uniform, in contrast to Ref. [19], which reported a dominant effect from the neutron $1f_{7/2}$ orbital via the SO potential. Our results indicate instead that the main reduction in $\Delta F_{\mathrm{CW}}^{48}$ due to the strong isovector tensor coupling originates from changes in the effective central potential.

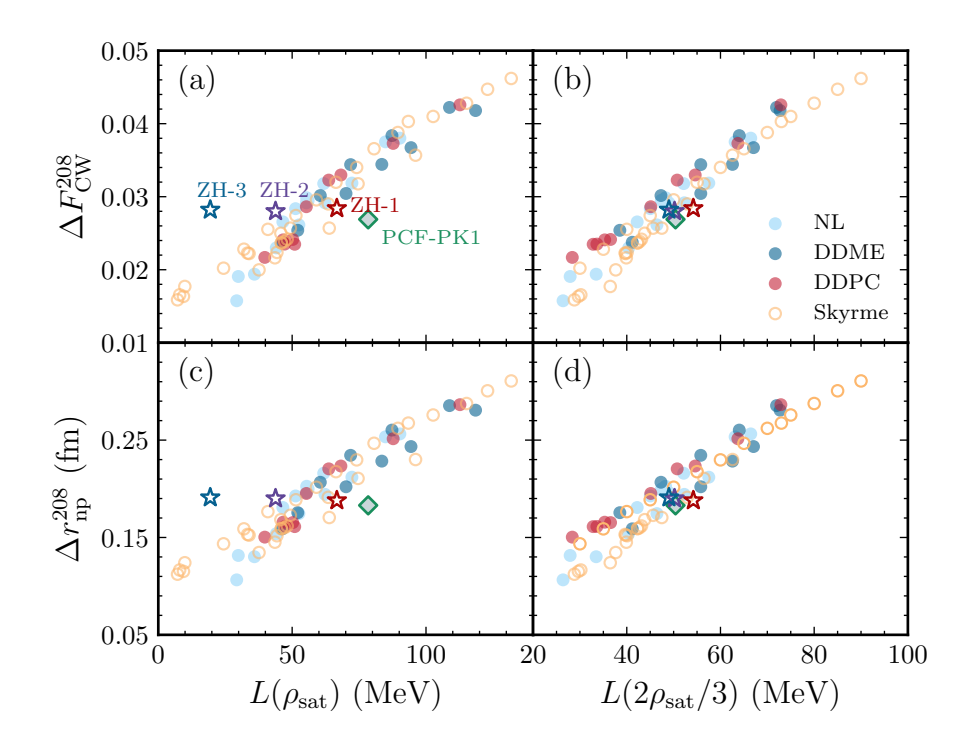


FIG. S7. Data-to-data relations between the charge-weak form factor difference $\Delta F_{\rm CW}$ in panels (a,b) and the neutron skin thickness $\Delta r_{\rm np}$ in panels (c,d) of ²⁰⁸Pb and the density-slope parameter of the symmetry energy, $L(\rho)$ at $\rho = \rho_{\rm sat}$ (left panels) and $\rho = 2\rho_{\rm sat}/3$ (right panels).

S.V. Correlations of ΔF_{cw} and Δr_{np} with the Symmetry Energy Slope at Different Densities

We show in Figs. S7 and S8 the data-to-data correlations between the charge-weak form-factor difference $\Delta F_{\rm CW}$ (upper panels) and the neutron skin thickness $\Delta r_{\rm np}$ (lower panels) of $^{208}{\rm Pb}$ and $^{48}{\rm Ca}$ with the density-slope parameter $L(\rho)$ of the symmetry energy evaluated at $\rho_{\rm sat}$ and $2\rho_{\rm sat}/3$. In addition to the ZH family and PCF-PK1, the comparison includes a broad set of relativistic and nonrelativistic EDFs. The relativistic EDFs comprise 16 nonlinear meson exchange (NL) models (FSU [24–26] and NL3 families [27, 28], IOPB-1 [29], IU-FSU [30], IU-FSU* [31], FSU-Garnet [29], BigApple [32]), 10 density-dependent meson-exchange (DDME) models (DD [33], DD2 [34], PK-DD [35], TW-99 [36], DDME1 [37], DDME2 [38], DDMEJ family [39]), and 13 density-dependent point-coupling (DDPC) models (DD-PCX [40], DDPC-PREX, DDPC-CREX, DDPC-REX [41], DD-PC1 [42], DD-PCJ family [43]). For completeness, 38 Skyrme EDFs are also included, such as SIII, SIV, SV, SVI [44], SLy230a, SLy230b, SLy4, SLy5, SLy8 [45, 46], SAMi [47], SGI, SGII [48], SkM [49], SkM* [50], Ska [51], MSk1, MSk2 [52], MSk7 [53], BSk1 [54], BSk2 [55], and the SkyLc family [56].

Although both relativistic and nonrelativistic conventional EDFs exhibit a strong correlation between $\Delta r_{\rm np}^{208}$ (or $\Delta F_{\rm CW}^{208}$) and slope parameter at saturation density $L(\rho_{\rm at})$, the ZH family shows a clear deviation. Despite large variations in $L(\rho_{\rm sat})$, the three ZH EDFs predict nearly identical values of $\Delta r_{\rm np}^{208}$ and $\Delta F_{\rm CW}^{208}$. This behavior indicates that the inclusion of a strong isovector tensor coupling can disrupt the conventional $\Delta r_{\rm np}^{208} - L(\rho_{\rm sat})$ correlation. Nevertheless, the correlation between $\Delta r_{\rm np}^{208}$ (or $\Delta F_{\rm CW}^{208}$) and $L(2\rho_{\rm sat}/3)$ remains robust. As for ⁴⁸Ca, $\Delta r_{\rm np}^{48}$ (or $\Delta F_{\rm CW}^{48}$) is also sensitive to IVSO interaction due to the eight SO unpaired neutron in $1f_{7/2}$. Consequently, as illustrated in Fig. S8,

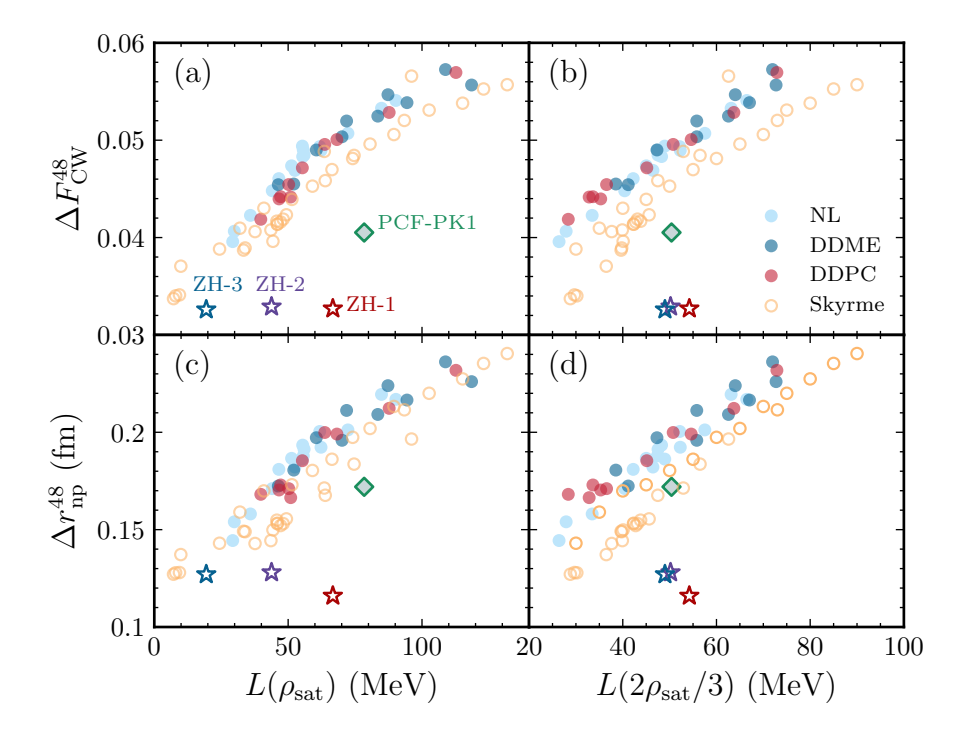


FIG. S8. Same as Figure S7, but for ⁴⁸Ca.

the ZH family exhibits a clear departure from the usual correlation between $\Delta r_{\rm np}^{48}$ (or $\Delta F_{\rm CW}^{48}$) and $L(2\rho_{\rm sat}/3)$.

[1] C. J. Horowitz and J. Piekarewicz, "Impact of spin-orbit currents on the electroweak skin of neutron-rich nuclei," Phys. Rev. C 86, 045503 (2012), arXiv:1208.2249 [nucl-th].

- [10] R. Machleidt and F. Sammarruca, "Recent advances in chiral EFT based nuclear forces and their applications," Prog. Part. Nucl. Phys. 137, 104117 (2024), arXiv:2402.14032 [nucl-th].
- [11] D. Adhikari et al. (CREX), "Precision Determination of the Neutral Weak Form Factor of Ca48," Phys. Rev. Lett. 129, 042501 (2022), arXiv:2205.11593 [nucl-ex].
- [12] D. Adhikari *et al.* (PREX), "Accurate Determination of the Neutron Skin Thickness of ²⁰⁸Pb through Parity-Violation in Electron Scattering," Phys. Rev. Lett. **126**, 172502 (2021), arXiv:2102.10767 [nucl-ex].
- [13] M. Wang, W. J. Huang, F. G. Kondev, G. Audi, and S. Naimi, "The AME 2020 atomic mass evaluation (II). Tables, graphs and references," Chin. Phys. C 45, 030003 (2021).
- [14] I. Angeli and K. P. Marinova, "Table of experimental nuclear ground state charge radii: An update," Atom. Data Nucl. Data Tabl. 99, 69-95 (2013).
- [15] F. Le Blanc et al., "Charge-radius change and nuclear moments in the heavy tin isotopes from laser spectroscopy: Charge

^[2] P.-G. Reinhard, X. Roca-Maza, and W. Nazarewicz, "Information Content of the Parity-Violating Asymmetry in Pb208," Phys. Rev. Lett. 127, 232501 (2021), arXiv:2105.15050 [nucl-th].

^[3] W. Xiong et al., "A small proton charge radius from an electron–proton scattering experiment," Nature 575, 147–150 (2019).

^[4] M. Tanabashi et al. (Particle Data Group), "Review of Particle Physics," Phys. Rev. D 98, 030001 (2018).

^[5] C. Alexandrou, S. Bacchio, M. Constantinou, J. Finkenrath, K. Hadjiyiannakou, K. Jansen, and G. Koutsou, "Nucleon strange electromagnetic form factors," Phys. Rev. D 101, 031501 (2020), arXiv:1909.10744 [hep-lat].

^[6] P. Klupfel, P. G. Reinhard, T. J. Burvenich, and J. A. Maruhn, "Variations on a theme by Skyrme: A systematic study of adjustments of model parameters," Phys. Rev. C 79, 034310 (2009), arXiv:0804.3385 [nucl-th].

^[7] N. Schwierz, I. Wiedenhover, and A. Volya, "Parameterization of the Woods-Saxon Potential for Shell-Model Calculations," (2007), arXiv:0709.3525 [nucl-th].

^[8] V. I. Isakov, K. I. Erokhina, H. Mach, M. Sanchez-Vega, and B. Fogelberg, "On the difference between proton and neutron spin orbit splittings in nuclei," Eur. Phys. J. A 14, 29–36 (2002), arXiv:nucl-th/0202044.

^[9] M. Qiu, B.-J. Cai, L.-W. Chen, C.-X. Yuan, and Z. Zhang, "Bayesian model averaging for nuclear symmetry energy from effective proton-neutron chemical potential difference of neutron-rich nuclei," Phys. Lett. B 849, 138435 (2024), arXiv:2312.07031 [nucl-th].

- radius of **132Sn," Phys. Rev. C 72, 034305 (2005).
- [16] D. Foreman-Mackey, D. W. Hogg, D. Lang, and J. Goodman, "emcee: The MCMC Hammer," Publ. Astron. Soc. Pac. 125, 306–312 (2013), arXiv:1202.3665 [astro-ph.IM].
- [17] H. H. Xie, J. Li, Y. L. Yang, and P. W. Zhao, "The charge radii of calcium isotopes within relativistic density functional theory: nucleon's finite-size and quadrupole shape fluctuation effects," (2025), 10.1103/1kbz-rx3m, arXiv:2508.09437 [nucl-th].
- [18] S. Huth, C. Wellenhofer, and A. Schwenk, "New equations of state constrained by nuclear physics, observations, and QCD calculations of high-density nuclear matter," Phys. Rev. C 103, 025803 (2021), arXiv:2009.08885 [nucl-th].
- [19] A. Kunjipurayil, J. Piekarewicz, and M. Salinas, "Role of the isovector spin-orbit potential in mitigating the CREX-PREX dilemma," Phys. Rev. C 112, 014310 (2025), arXiv:2503.07405 [nucl-th].
- [20] P. G. Reinhard, "The relativistic mean-field description of nuclei and nuclear dynamics," Reports on Progress in Physics 52, 439 (1989).
- [21] A. Sulaksono, T. Burvenich, J. A. Maruhn, P. G. Reinhard, and W. Greiner, "The Nonrelativistic limit of the relativistic point coupling model," Annals Phys. 308, 354–370 (2003), arXiv:nucl-th/0305078.
- [22] A. Sulaksono, T. J. Burvenich, P. O. Hess, and J. A. Maruhn, "Nonrelativistic limit of point-coupling model," Int. J. Mod. Phys. E 20, 139–163 (2011).
- [23] T.-G. Yue, Z. Zhang, and L.-W. Chen, "PREX and CREX: Evidence for Strong Isovector Spin-Orbit Interaction," (2024), arXiv:2406.03844 [nucl-th].
- [24] B. G. Todd-Rutel and J. Piekarewicz, "Neutron-Rich Nuclei and Neutron Stars: A New Accurately Calibrated Interaction for the Study of Neutron-Rich Matter," Phys. Rev. Lett. 95, 122501 (2005), arXiv:nucl-th/0504034.
- [25] W.-C. Chen and J. Piekarewicz, "Building relativistic mean field models for finite nuclei and neutron stars," Phys. Rev. C 90, 044305 (2014), arXiv:1408.4159 [nucl-th].
- [26] J. Piekarewicz, "Pygmy Resonances and Neutron Skins," Phys. Rev. C 83, 034319 (2011), arXiv:1012.1803 [nucl-th].
- [27] G. A. Lalazissis, J. Konig, and P. Ring, "A New parametrization for the Lagrangian density of relativistic mean field theory," Phys. Rev. C 55, 540–543 (1997), arXiv:nucl-th/9607039.
- [28] C. J. Horowitz and J. Piekarewicz, "Constraining URCA cooling of neutron stars from the neutron radius of Pb-208," Phys. Rev. C 66, 055803 (2002), arXiv:nucl-th/0207067.
- [29] T. Miyatsu, M.-K. Cheoun, K. Kim, and K. Saito, "Can the PREX-2 and CREX results be understood by relativistic mean-field models with the astrophysical constraints?" Phys. Lett. B 843, 138013 (2023), arXiv:2303.14763 [nucl-th].
- [30] F. J. Fattoyev and J. Piekarewicz, "Relativistic models of the neutron-star matter equation of state," Phys. Rev. C 82, 025805 (2010), arXiv:1003.1298 [nucl-th].
- [31] B. K. Agrawal, A. Sulaksono, and P. G. Reinhard, "Optimization of relativistic mean field model for finite nuclei to neutron star matter," Nucl. Phys. A 882, 1–20 (2012), arXiv:1204.2644 [nucl-th].
- [32] F. J. Fattoyev, C. J. Horowitz, J. Piekarewicz, and B. Reed, "GW190814: Impact of a 2.6 solar mass neutron star on the nucleonic equations of state." Phys. Rev. C 102, 065805 (2020), arXiv:2007.03799 [nucl-th].
- [33] S. Typel, "Relativistic model for nuclear matter and atomic nuclei with momentum-dependent self-energies," Phys. Rev. C 71, 064301 (2005), arXiv:nucl-th/0501056.
- [34] S. Typel, G. Ropke, T. Klahn, D. Blaschke, and H. H. Wolter, "Composition and thermodynamics of nuclear matter with light clusters," Phys. Rev. C 81, 015803 (2010), arXiv:0908.2344 [nucl-th].
- [35] W.-h. Long, J. Meng, N. Van Giai, and S.-G. Zhou, "New effective interactions in RMF theory with nonlinear terms and density dependent meson nucleon coupling," Phys. Rev. C 69, 034319 (2004), arXiv:nucl-th/0311031.
- [36] S. Typel and H. H. Wolter, "Relativistic mean field calculations with density dependent meson nucleon coupling," Nucl. Phys. A 656, 331–364 (1999).
- [37] T. Niksic, D. Vretenar, P. Finelli, and P. Ring, "Relativistic Hartree-Bogolyubov model with density dependent meson nucleon couplings," Phys. Rev. C 66, 024306 (2002), arXiv:nucl-th/0205009.
- [38] G. A. Lalazissis, T. Niksic, D. Vretenar, and P. Ring, "New relativistic mean-field interaction with density-dependent meson-nucleon couplings," Phys. Rev. C 71, 024312 (2005).
- [39] D. Vretenar, T. Niksic, and P. Ring, "A Microscopic estimate of the nuclear matter compressibility and symmetry energy in relativistic mean field models," Phys. Rev. C 68, 024310 (2003), arXiv:nucl-th/0302070.
- [40] E. Yuksel, T. Marketin, and N. Paar, "Optimizing the relativistic energy density functional with nuclear ground state and collective excitation properties," Phys. Rev. C 99, 034318 (2019), arXiv:1901.05552 [nucl-th].
- [41] E. Yüksel and N. Paar, "Implications of parity-violating electron scattering experiments on 48Ca (CREX) and 208Pb (PREX-II) for nuclear energy density functionals," Phys. Lett. B 836, 137622 (2023), arXiv:2206.06527 [nucl-th].
- [42] T. Niksic, D. Vretenar, and P. Ring, "Relativistic Nuclear Energy Density Functionals: Adjusting parameters to binding energies," Phys. Rev. C 78, 034318 (2008), arXiv:0809.1375 [nucl-th].
- [43] E. Yüksel, T. Oishi, and N. Paar, "Nuclear Equation of State in the Relativistic Point-Coupling Model Constrained by Excitations in Finite Nuclei," Universe 7, 71 (2021).
- [44] M. Beiner, H. Flocard, N. van Giai, and P. Quentin, "Nuclear ground state properties and selfconsistent calculations with the Skyrme interactions: 1. Spherical description," Nucl. Phys. A 238, 29–69 (1975).
- [45] E. Chabanat, J. Meyer, P. Bonche, R. Schaeffer, and P. Haensel, "A Skyrme parametrization from subnuclear to neutron star densities," Nucl. Phys. A 627, 710-746 (1997).
- [46] E. Chabanat, P. Bonche, P. Haensel, J. Meyer, and R. Schaeffer, "A Skyrme parametrization from subnuclear to neutron star densities. 2. Nuclei far from stablities," Nucl. Phys. A 635, 231–256 (1998), [Erratum: Nucl.Phys.A 643, 441–441 (1998)].

- [47] X. Roca-Maza, G. Colo, and H. Sagawa, "A new Skyrme interaction with improved spin-isospin properties," Phys. Rev. C 86, 031306 (2012), arXiv:1205.3958 [nucl-th].
- [48] N. van Giai and H. Sagawa, "Spin-isospin and pairing properties of modified Skyrme interactions," Phys. Lett. B 106, 379–382 (1981).
- [49] H. Krivine, J. Treiner, and O. Bohigas, "Derivation of a fluid-dynamical lagrangian and electric giant resonances," Nucl. Phys. A 336, 155–184 (1980).
- [50] J. Bartel, P. Quentin, M. Brack, C. Guet, and H. B. Hakansson, "Towards a better parametrisation of Skyrme-like effective forces: A Critical study of the SkM force," Nucl. Phys. A 386, 79–100 (1982).
- [51] H. S. Köhler, "Skyrme force and the mass formula," Nucl. Phys. A 258, 301–316 (1976).
- [52] F. Tondeur, S. Goriely, J. M. Pearson, and M. Onsi, "Towards a Hartree-Fock mass formula," Phys. Rev. C 62, 024308 (2000).
- [53] S. Goriely, F. Tondeur, and J. M. Pearson, "A Hartree-Fock Nuclear Mass Table," Atom. Data Nucl. Data Tabl. 77, 311–381 (2001).
- [54] M. Samyn, S. Goriely, P. H. Heenen, J. M. Pearson, and F. Tondeur, "A Hartree–Fock–Bogoliubov mass formula," Nucl. Phys. A 700, 142–156 (2002).
- [55] S. Goriely, M. Samyn, P. H. Heenen, J. M. Pearson, and F. Tondeur, "Hartree-fock mass formulas and extrapolation to new mass data," Phys. Rev. C 66, 024326 (2002).
- [56] T.-G. Yue, L.-W. Chen, Z. Zhang, and Y. Zhou, "Constraints on the symmetry energy from PREX-II in the multimessenger era," Phys. Rev. Res. 4, L022054 (2022), arXiv:2102.05267 [nucl-th].